Energy Storage Materials 89 (2026) 105167

Contents lists available at ScienceDirect

Energy Storage Materials

journal homepage: www.elsevier.com/locate/ensm

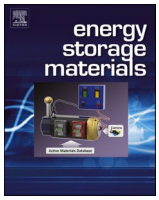

# Enhanced interfacial stability and electrochemical performance via cathode-adhesion-enhanced coatings for all-solid-state batteries

Junseong Kim [a,b,1], Hoseok Lee [a,c,1], Taegyu Kim [a,b], Eunyoung Ryu [a,b], Imsul Seo [d], Ju Yeong Seong [d], Chungbum Lim [d], Jongsoon Kim [a,b,c,*]

[a] Department of Energy Science, Sungkyunkwan University, Suwon 16419, Republic of Korea
[b] SKKU Institute of Energy Science and Technology (SIEST), Sungkyunkwan University, Suwon 16419, Republic of Korea
[c] Department of Future Energy Engineering, Sungkyunkwan University, Suwon 16419, Republic of Korea
[d] Hyundai Motor Company, Uiwang 16082, Republic of Korea

ARTICLE INFO

*Keywords:*
All-solid-state-battery
Cathode coating material
Bonding interaction
Cathode interface
First-principles calculation

ABSTRACT

All-solid-state batteries (ASSBs) suffer from poor interfacial adhesion betweenthe Ni-rich NCM cathode and conventional coatings (CCs) such as $LiNbO_3$, resulting in poor rate- and cycle-performances. Through first-principles calculations, we identify that the interfacial adhesion is weakened during the delithiation process, which can lead to coating exfoliation and direct contact with the sulfide-based solid electrolyte. To address this issue, we design a cathode–adhesion-enhanced coating (CAEC) that strengthens bonding interactions and oxygen affinity within the crystal structure of the conventional coating, $LiNbO_3$. CAEC also provides a lower activation barrier for $Li^+$ transport and a wider electrochemical potential window than the CCs, indicating CAEC not only enhances cycle-performances but also improves power-capability and high-voltage operation stability. As a result, CAEC-applied ASSBs deliver highly enhanced initial Coulombic efficiency, power-capability and cycle-performance compared to CC-applied ASSBs. Furthermore, in terms of cycle-performance, CAEC-applied ASSBs not only maintain their capacity but also exhibit reduced voltage-decay, demonstrating a clear advantage in retaining energy density during prolonged cycling. The application of CAEC effectively and stably suppresses interfacial side reactions between the sulfide-based solid electrolyte and the Ni-rich NCM cathodes during prolonged cycling, highlighting its significant advantage in mitigating the intrinsic degradation issues of ASSBs.

## 1. Introduction

The growing demand for sustainable and environmentally friendly energy storage drives the rapid advancement of lithium-ion batteries (LIBs), in which organic liquid electrolytes have enabled the widespread electrification of portable electronics and electric vehicles [1]. Their high energy density, excellent cyclability, and well-established manufacturing processes have further accelerated their global adoption [2–4]. Nevertheless, LIBs still face intrinsic challenges, particularly regarding the limited practical energy density and the use of flammable organic electrolytes, which can cause serious safety hazards under mechanical deformation or thermal runaway conditions [5–8].

All-solid-state batteries (ASSBs) have thus emerged as a promising next-generation energy storage technology, offering improved intrinsic safety through the use of non-flammable, flame-retardant solid electrolytes (SEs) [9–11]. In addition to enhanced safety, ASSBs offer the potential for higher energy densities by enabling the use of high-capacity lithium metal anodes, which are otherwise impractical in conventional LIB systems due to safety concerns [12–14]. Moreover, the absence of a conventional separator facilitates compact and efficient cell architecture [15]. Among various SE candidates, sulfide-based SEs have garnered significant attention due to their high lithium-ion conductivity (>1 mS $cm^{-1}$), comparable to that of carbonate-based liquid electrolytes [16–21]. Their excellent ductility also facilitates intimate interfacial contact with electrode particles, enhancing processability.

Recent studies have focused on the integration of sulfide-based SEs with Ni-rich NCM cathodes ($Li[Ni_xCo_yMn_z]O_2$, $x \geq 0.6$, $x + y + z = 1$) to achieve both high energy density and long-term cycling stability [22–24]. However, the direct contact between sulfide SEs and cathode materials still presents major interfacial challenges, including

* Corresponding author.
*E-mail address:* jongsoonkim@skku.edu (J. Kim).
[1] These authors contribute equally to this work.

https://doi.org/10.1016/j.ensm.2026.105167
Received 2 March 2026; Received in revised form 15 April 2026; Accepted 26 April 2026
Available online 27 April 2026

undesirable side reactions, increased resistance, and accelerated capacity fading [25,26]. Additionally, electrochemical potential mismatch induces the formation of a space charge layer (SCL), which inhibits $Li^+$ transport across the interface, thereby degrading the overall performance of ASSBs [27–29].

To mitigate these interfacial issues, conventional coatings (CCs) (i.e. $LiNbO_3$) have been widely explored due to their high ionic conductivity and chemical compatibility with both the cathode and sulfide electrolyte [30,31]. CCs help suppress the formation of interfacial resistance and maintain lithium-ion conduction at the cathode–electrolyte boundary [32–35]. Nevertheless, recent findings indicate that CCs suffer from mechanical and electrochemical instability during extended cycling [36,37]. Structural changes in the Ni-rich $Li[Ni_{0.8}Co_{0.1}Mn_{0.1}]O_2$ (NCM811) cathode and dynamic variation in the oxidation states of transition metal ions can compromise the coating's adhesion to the cathode surface, leading to delamination [38–41]. Moreover, CCs are susceptible to decomposition under high-voltage operation, releasing lithium and oxygen species [42,43]. These decomposition products may react with the sulfide SE, forming $PO_x$ and $SO_x$ by-products that further deteriorate interfacial stability [44–46].

To address these limitations while preserving the functional merits of CCs, we focused on developing a strategy that enables the coating layer to maintain stronger interfacial adhesion with the cathode during charge/discharge while simultaneously achieving a wider electrochemical stability window. To verify the performance enhancement through improved oxygen affinity and strengthened overall bonding interactions within the bulk structure of CCs, Mg–O bonding was introduced into the well-known $LiNbO_3$ (LNO) coating, replacing part of the Li–O bonds. This strategy reinforces the lattice bonding strength and increases the oxygen affinity through multivalent charge compensation induced by Mg–O bond formation. Through first-principles calculations, it was revealed that a cathode-adhesion-enhanced coating (CAEC), $[Li_{0.9}Mg_{0.05}]NbO_3$ ($Mg_{0.05}$-LNO), exhibited highly enhanced adhesion with NCM811 cathode during delithiation compared to a CC, indicating effective suppression of coating delamination and enhancing cycle-performance of NCM811-based ASSBs. Moreover, CAEC was found to possess improved $Li^+$ transport properties and a wider electrochemical stability window than the CC, which can enhance the power capability and stabilize the high-voltage charging process of NCM811-based ASSBs.

Consistent with theoretical predictions, CAEC-applied ASSBs (CAEC@ASSBs) delivered significantly improved initial capacity, higher initial Coulombic efficiency, and enhanced power capability compared to the CC-applied ASSBs (CC@ASSBs). At C/10 (1C = 185 mA $g^{-1}$), the CAEC@ASSB delivered an initial discharge capacity of 202.30 mAh $g^{-1}$ and an initial Coulombic efficiency of 91.7%, both of which are higher than those of the CC@ASSBs (195.99 mAh $g^{-1}$ and 90.4%, respectively). Moreover, the CAEC@ASSB showed outstanding rate performance, retaining 73.4% of its C/10 capacity under 2C operation (146.78 mAh $g^{-1}$), outperforming the CC@ASSBs. Notably, after 100 cycles at C/2, CAEC@ASSB retained 81.0% of its initial capacity, whereas CC@ASSB exhibited only 74.2% retention at the same condition, demonstrating improved interfacial stability enabled by the application of CAEC in the ASSB system.

ToF-SIMS analysis confirmed that CAEC effectively suppresses the formation of chemical interfacial degradation products compared to CC, highlighting its role in mitigating chemical side reactions at the cathode–electrolyte interface. In addition, *ex-situ* XRD analysis confirmed that the improved interfacial adhesion between CAEC and NCM811 cathode can successfully suppress structural degradation, such as contact loss caused by volume changes during cycling, thereby maintaining interfacial mechanical stability and contributing to enhanced electrochemical performance. These findings highlight the importance of precisely controlling cathode–coating adhesion to enable high-performance and stable ASSBs.

## 2. Material and methods

### 2.1. Materials preparation

Commercial $Li[Ni_{0.8}Co_{0.1}Mn_{0.1}]O_2$ (NCM811) and $Li[Ni_{0.9}Co_{0.05}Mn_{0.05}]O_2$ (NCM955), supplied by Hyundai Motors, were used as uncoated samples. $LiNbO_3$ (LNO) and $[Li_{0.9}Mg_{0.05}]NbO_3$ ($Mg_{0.05}$-LNO) coatings were prepared via the same wet chemical methods under identical processing conditions, using lithium ethoxide (Sigma Aldrich, 95%), niobium ethoxide (Sigma Aldrich, 99.9%), and magnesium ethoxide (Sigma Aldrich, 98%). The coating loading was fixed at 1 wt% relative to the cathode powder mass for both LNO (CC) and $Mg_{0.05}$-LNO (CAEC) as the optimized condition. For comparison, additional CAEC-coated NCM811 (CAEC-NCM811) samples with coating loadings of 0.5 wt% and 2 wt% CAEC were also prepared using the same synthesis procedure as that used for CC-coated NCM811 (CC-NCM811) to evaluate the effect of coating loading. Each precursor was used in stoichiometric proportions to ensure accurate composition during the synthesis process. In 20 mL of anhydrous ethyl alcohol, 5 g of NCM powder was mixed with 20 mL of a 1 wt% coating solution and stirred at 70 °C until it evaporated sufficiently. For the 0.5 wt% and 2 wt% coating conditions, the precursor concentration was adjusted while maintaining the same overall synthesis procedure. The resulting powder was dried in a vacuum oven at 80 °C overnight and then calcined at 300 °C for 5 h in an oxygen atmosphere. The CAEC-NCM811 sample prepared at 300 °C for 5 h was denoted as low-crystalline CAEC, whereas the sample additionally calcined at 600 °C for 5 h was denoted as high-crystalline CAEC. In addition, CAEC was also applied to NCM955 using the same 1 wt% coating condition and synthesis procedure to evaluate the broader applicability of the CAEC strategy. Bulk powders of LNO and $Mg_{0.05}$-LNO were synthesized using a higher concentration of the coating solution via the same synthesis procedure.

### 2.2. Materials characterization

The crystal structures of CC- and CAEC-NCM811 cathodes, including samples with different coating loadings (0.5, 1, and 2 wt%) and different crystallinities (low and high), as well as CAEC-NCM955 and argyrodite-type sulfide electrolyte of $Li_6PS_5Cl_{0.5}Br_{0.5}$ were analyzed using an X-ray diffractometer (PANalytical Empyrean) with Mo Kα radiation (λ = 0.790319 Å) in a 2θ range of 5.01° to 34.99° with step size of 0.015° For comparison with other studies, the 2θ angles of XRD patterns were converted to Cu Kα radiation (λ=1.54178 Å). Rietveld refinement was carried out using FullProf software. *Ex-situ* X-ray diffraction (XRD) analysis was carried out to monitor the structural evolution of the composite cathode electrodes at various electrochemical states. The electrodes were recovered from cells at the following states: pristine (as-prepared), discharged to 2.5 V in the 1st cycle, and discharged to 2.5 V after 100 cycles. After cycling, the cells were disassembled in an argon-filled glovebox. For XRD analysis, $Li_6PS_5Cl_{0.5}Br_{0.5}$ and composite electrode samples were sealed with a domed sample holder to prevent air and moisture exposure. *Ex-situ* XRD patterns were analyzed by fitting the selected reflections of (003), (101), and (104) using a Voigt profile. The full width at half maximum (FWHM) values were obtained in degrees of $2\theta$ and converted to radians as $\beta$ = FWHM × $\pi$/180.

$$\beta\cos\theta = \frac{K\lambda}{D} + 4\varepsilon\sin\theta \quad (1)$$

where $\theta$ is the Bragg angle, λ is the X-ray wavelength (Cu K$\alpha$, λ = 1.5406 Å), K is the shape factor (K = 0.9), and ε is the microstrain. For each electrochemical state, the W–H plot was constructed using $x = 4\sin\theta$ and $y = \beta\cos\theta$, and ε (slope) was obtained by least-squares linear regression. Field-emission scanning electron microscopy (FE-SEM; Gemini SEM 560, ZEISS) was used to investigate particle morphology and particle size of LNO, $Mg_{0.05}$-LNO coated NCM powder. Scanning electron

microscopy-energy dispersive X-ray spectroscopy (EDS) mapping were conducted to analyze distribution and quantification of elements at the national Center for Inter-University Research Facilities (NCIRF) at Seoul national University. Inductively coupled plasma-optical emission spectroscopy (ICP-OES; Thermo Fisher Scientific, iCAP Pro) analysis of the coated cathode powders was performed at the Yonsei University Core Instrument Center. Prior to the measurement, the samples were digested with an HF-containing acid solution because niobium is a fluoride-soluble element and requires HF pretreatment for complete dissolution. Before FIB milling process, the NCM811 cathode samples were embedded in an epoxy resin to mechanically stabilize the electrode and ensure structural integrity during ion beam processing. The embedded samples were then polished to expose a flat surface and mounted on standard FIB stubs for cross-sectional analysis. Subsequent milling and imaging were conducted using a JIB-4601F focused ion beam system (JEOL Ltd., Japan), which integrates a high-power Ga ion source with a Schottky-type field emission scanning electron microscope (SEM). Coarse milling was carried out at 30 kV and 10 na, followed by fine polishing at 5 kV and 1 na to minimize beam-induced damage. Prior to milling, a Pt protective layer was deposited via the gas injection system (GIS) to preserve the surface morphology. All operations were performed under high vacuum conditions. Cross-sections were observed in situ using the SEM at 5 kV, allowing for detailed analysis of the cathode microstructure, including intergranular features and interface stability.

High-resolution scanning transmission electron microscopy (HR-STEM) images and energy-dispersive X-ray spectroscopy (EDS) mappings were acquired using a 300 kV STEM (JEM-ARM300F, JEOL) at the Advanced Facility Center for Quantum Technology at Sungkyunkwan University. Nb K-edge spectra were collected in transmission mode over an energy range of 18,784 ~ 19,954 eV at the 10C Wide XAFS beamline at Pohang Accelerator Laboratory (PAL). Reference spectra were simultaneously obtained using Nb metal foil. The collected XAS data were analyzed using Athena software. Each sample was prepared in the form of a powder. Time-of-Flight Secondary Ion Mass Spectrometry (TOF-SIMS) analysis was performed using a TOF.SIMS 5 instrument (ION-TOF GmbH, Germany) to investigate the elemental distributions and interfacial chemical changes at the national Center for Inter-University Research Facilities (NCIRF) at Seoul national University. Both 3D chemical imaging and depth profiling were conducted under negative and positive polarity mode. For 3D mapping, a $Bi_3^{2+}$ primary ion beam with an energy of 60 keV and a current of 0.1 pA was rastered over a 100 × 100 $um^2$ area. The data were acquired at a resolution of 1024 × 1024 pixels and binned to 256 × 256 pixels for analysis. The charge compensation during analysis was achieved using a low-energy electron flood gun. Depth profile analysis was conducted using dual-beam mode. A $Bi^+$ analysis beam (30 keV, 1 pA) was used for signal acquisition, while a $Cs^*$ sputter beam (500 eV, 40 nA) was rastered over a 400 × 400 $um^2$ area for etching. Based on the accumulated sputter ion dose (SpIDD = 1.55 × $10^{17}$ ions $cm^{-2}$) and typical sputter yields for inorganic solids under low-energy $Cs^+$ bombardment, the removed thickness is estimated to be on the order of several tens of nanometers (30–100 nm). Notably, because the depth profiling was performed on a mixed composite cathode (coated NCM811 : S-SE : carbon : binder = 70 : 29 : 1 : 1) rather than a planar layered stack, the analyzed 100 × 100 $um^2$ region inherently contains cathode particle surfaces/near-surface bulk, interphase domains, and S-SE regions simultaneously within this shallow sputter depth. Therefore, the depth profile is interpreted in terms of sputter-time regimes defined by the overlap of cathode- and S-SE-related marker ions, rather than a strict one-dimensional layer thickness assignment. AFM-based modulus mapping was conducted using an atomic force microscope (NX-10, park Systems) operated in PinPoint nanomechanical mapping mode. Force-distance curves were acquired at each pixel over an area of 8 × 8 $um^2$. The apparent Young's modulus was extracted by fitting the force–distance curves with a standard contact-mechanics model implemented in the analysis software. Instrumented nanoindentation was performed using a nanoTest Vantage system (Micro Materials) to evaluate indentation hardness (H) and reduced modulus ($E_r$) . Indentations were carried out on the top surface of the electrodes under identical conditions with a maximum load of 20 mN. The load-displacement curves were analyzed using the Oliver–Pharr method to obtain H and $E_r$. For each sample, 10 independent indents were performed at different locations. Nb 3*d* and Mg 2*p* XPS analyses were performed using a SUPRA+ (Kratos Analytical) for composite cathodes of CC and CAEC in the pristine and 100-cycled states. All sample handling and transfer were conducted without air exposure using a glovebox-based process. All XPS spectra were charge-corrected by referencing the C 1*s* peak to 284.8 eV.

### 2.3. Electrochemical characterization

To prepare LNO- and $Mg_{0.05}$-LNO-coated NCM811 composite cathodes, 70 wt% active material, 29 wt% $Li_6PS_5Cl_{0.5}Br_{0.5}$, 1 wt% Super P carbon black, and 1 wt% nitrile butadiene rubber (nBR) dissolved in normal butyl butyrate were mixed using Pulverisette 23 from Fritsch. For comparative electrochemical evaluation, composite cathodes were prepared using CAEC-NCM811 with different coating loadings (0.5, 1, and 2 wt%) and crystallinities (low and high), as well as CAEC-NCM955, following the same procedure. The mixture was cast on carbon-coated aluminum foil with a thickness of 250 um and dried overnight at 150 °C under vacuum conditions. The electrode was then punched into a disk of 12 mm diameter, with a mass loading of cathode material about ~15 mg $cm^{-2}$. As a counterpart electrode, 0.1 mm-thick Li metal was punched into a 12 mm diameter disk. All electrode preparation steps were conducted in a dry-room environment with a dew point of −60 °C. For the various galvanostatic tests of solid-state batteries, the pressurization cells were assembled by using all components. The electrolyte of $Li_6PS_5Cl_{0.5}Br_{0.5}$ was pelletized in Teflon cell body with a diameter of 13 mm under a pressure of 12 MPa for 1 min using RIKEN Mini Press (CDM-10PA). The cathode composite electrode was placed on one side of the formed electrolyte pellet and pressed at 45 MPa for 1 min. Then, a Li metal anode was placed on the opposite side, and constant pressure was applied by fastening the cap with a torque of 5 N•m. All cell assembly steps were performed in an Ar-filled glovebox with $O_2$ and $H_2O$ levels maintained below 1 ppm. Galvanostatic charge/discharge tests were conducted at different current densities from C/10 to 2C rate within a voltage range of 2.5–4.25 V (vs. $Li^+$/Li). The current density of 1C rate was set to 185 mA $g^{-1}$ for $Mg_{0.05}$-LNO, LNO coated NCM and bare NCM. Tests were performed using an automatic battery charge/discharge test system (WBCS 3000, WonATech). Rate capability tests were performed with charging at C/10 in CC/CV mode, where the constant voltage step was applied at 4.25 V until the current decreased to 0.05 C. The discharge current densities were set to 0.1, 0.2, 0.33, 0.5, 1, and 2 C. The cycling performance was evaluated over a voltage range of 2.5–4.25 V for 100 cycles, and 2.5–4.35 V for 50 cycles at a current density of C/2. Charging was conducted in CC/CV mode, where the constant voltage step was maintained until the current decreased to the cut-off value. All electrochemical tests were conducted inside an Ar-filled glovebox maintained at 30 °C with $O_2$ and $H_2O$ levels below 1 ppm, thereby minimizing any external exposure and excluding air/moisture-related effects as much as possible. Galvanostatic intermittent titration technique (GITT) analyses of the electrodes were performed at a current density of C/10 with 10 min of charge/discharge and 30 min of rest for each step. The $Li^+$ ionic conductivity of $Li_6PS_5Cl_{0.5}Br_{0.5}$ sulfide solid electrolyte, CC bulk, and CAEC bulk were evaluated by EIS using pelletized samples. Pellets were prepared for 150 mg of each powder 13 mm-diameter Teflon cell body at 45 MPa for 1 min using a RIKEN Mini Press (CDM-10PA). Subsequently, constant pressure was maintained by fastening the cap with a torque of 10 N·m. $Li^+$ ion conductivity ($\sigma Li^+$) was calculated by using the following equation expressed as:

$\sigma Li^+ = \frac{1}{R} \times \frac{d}{A}$(*R*: radius of pellet, *d*: thickness of pellet, *A*: area of pellet) (1)

Electrochemical impedance spectroscopy (EIS) was carried out using a potentiostatic mode to evaluate the ionic conductivity of the solid electrolyte. The impedance spectra were measured over a frequency range from 1 MHz to 1 Hz with a logarithmic sweep type. The applied AC amplitude was set to 10 mV with a bias potential of 0 V. The sample was stabilized for 3 min prior to measurement, and the stability criterion was set at $1.0 \times 10^{-3}$ V $s^{-1}$. Each measurement was conducted with a density of 10 points per decade and a single iteration. To evaluate the oxidative stability of the coating materials, linear sweep voltammetry (LSV) measurements were performed using pelletized bulk $Mg_{0.05}$-LNO and pristine LNO samples assembled in stainless steel | sample pellet | Li metal cell configuration. The voltage was swept from open-circuit voltage (OCV) to 5.0 V (vs. $Li^+$/Li) at a scan rate of 0.1 mV $s^{-1}$.

### 2.4. Computational details

First-principles calculations were performed using the Vienna Ab Initio Simulation package (VASP) [47]. The Generalized Gradient Approximation (GGA) with the Perdew–Burke–ERNZERHOF (PBE) functional was applied, in combination with the projector-augmented wave (PAW) method [48,49]. The GGA+U method was employed to account for the localized nature of the *d*-orbitals in Ni (U = 6.0 eV), Co (U = 3.4 eV), and Mn (U = 3.9 eV), with U values derived from a previous study [50]. A plane-wave cutoff energy of 500 eV was applied, and the geometry of both bulk LNO and $Mg_x$-LNO structures were fully optimized until the atomic forces were below 0.04 eV/Å. For the DFT calculations, a 2 × 2 × 1 Γ-centered k-point grid was used for Brillouin zone sampling to calculate the supercell structures of both compounds. Nudged elastic band (NEB) simulations were performed to determine the $Li^+$ diffusion energy barriers in bulk LNO and $Mg_x$-LNO [51].

To investigate the electrochemical stability of coating materials, we constructed a grand potential phase diagram. This diagram, generated using Pymatgen, illustrates the phase equilibria of the material in equilibrium with a lithium reservoir characterized by a chemical potential, $\mu_{Li}$. Following previous studies, the applied electrostatic potential (ϕ) was incorporated into the lithium chemical potential $\mu_{Li}$, expressed as:

$$\mu_{Li}(\phi) = \mu_{Li}^0 - e\phi \tag{2}$$

where $\mu Li_0$ represents the chemical potential of lithium metal, and the potential ϕ is referenced against lithium metal in this work [52,53].

The materials LNO, $Mg_x$-LNO, LPSCB, and NCM811 represent $LiNbO_3$, $[Li_{1-2x}Mg_x]NbO_3$, $Li_6PS_5Cl_{0.5}Br_{0.5}$, and $Li[Ni_{0.8}Co_{0.1}Mn_{0.1}]O_2$, respectively. The LNO@NCM811 surface structure is formed by the (100) surface of LNO and the (100) surface of NCM811 [29]. Similarly, the LNO-LPSCB surface structure is formed by the (100) surface of LNO and the (010) surface of LPSCB. Additionally, Mg doping was applied to the LNO surface model, taking charge balance into account.

The surface adhesion energy is defined as:

$$\Delta E_{ads} = \Delta E_{substrate@coatingmaterial} - \Delta\left[E_{substrate} + E_{coatingmaterial}\right] \tag{3}$$

Where $\triangle E_{substrate@coating\ material}$ is the total energy of the surface model with LNO and $Mg_x$-LNO, $\triangle E_{substrate}$ is the energy of the NCM811 or LPSCB, and $\triangle E_{coating\ material}$ is the energy of the coating material binding to the bulk NCM811 or LPSCB [53–55]. The Brillouin zone integration of LNO@NCM811/$Mg_x$-LNO@NCM811 and LNO@LPSCB/$Mg_x$-LNO@LPSCB was performed using a 3 × 2 × 1 Γ-centered k-point grid and a 2 × 3 × 1 Γ-centered k-point grid, respectively. The cutoff energy for all surface models using plane waves was set to 500 eV. The convergence criteria for both electronic and ionic optimizations were set to $1 \times 10^{-4}$ eV and 0.03 eV/Å, respectively. The crystal structures were depicted using VESTA software [56].

## 3. Results and discussion

### 3.1. Strategy to improve interfacial adhesion between Ni-rich layered cathode and coatings

To improve interfacial adhesion of coatings with NCM811 cathode, we focused on strengthening bonding interaction and oxygen affinity in the bulk structure of conventional coatings (CCs), $LiNbO_3$ (LNO). We expected that incorporating ions with similar ionic radii to $Li^+$ but higher oxidation states (i.e., $Mg^{2+}$) into the bulk structure of the coating layer would provide stronger affinity with oxygen ions than $Li^+$, thereby maintaining robust interfacial adhesion with the cathode even during charge and discharge. To verify this, we investigated the variation in adhesion energy between the NCM811 cathode surface and the coating layer upon $Li^+$ delithiation through first-principles calculations (Fig. 1a). Based on this model, we systematically evaluated the adhesion energies between the coating material and the NCM cathode across various states of charge (SoC) to simulate practical charge–discharge conditions.

As shown in Fig. 1b and Table S1, the calculated adhesion energies for LNO-coated $Li_y[Ni_{0.8}Co_{0.1}Mn_{0.1}]O_2$ (denoted as LNO@$Li_y$NCM, where *y* represents the lithium content; *y* = 1, 2/3, 1/3, 0) and $[Li_{1-2x}Mg_x]NbO_3$-coated $Li_y[Ni_{0.8}Co_{0.1}Mn_{0.1}]O_2$ (denoted as $Mg_x$-LNO@$Li_y$NCM) are summarized. LNO@$Li_y$NCM showed a progressive reduction in adhesion energies with decreasing SoC, indicating a weakening of coating–cathode adhesion during extended cycling. In contrast, $Mg_{1/12}$-LNO@$Li_y$NCM maintains consistently stronger adhesion across all SoC levels, with higher adhesion energies than those of LNO. Notably, even under deep delithiation (e.g., $Li_{1/3}$ and $Li_0$ states), the $Mg_x$-LNO@$Li_y$NCM coatings exhibited robust interfacial binding, indicating improved resistance to delamination and better interfacial stability throughout cycling. However, $Mg_{2/12}$-LNO@$Li_y$NCM with higher Mg contents exhibited poor adhesion with NCM811 cathode compared to LNO@$Li_y$NCM at most SoC levels. In the DFT-derived thermodynamically stable interfacial configurations, the NCM–coating separation increases with Mg content in LNO (Fig. S1), reducing the effective interfacial contact and thereby weakening adhesion. In addition, the interface-local Nb–O bonding environment becomes increasingly heterogeneous with higher Mg contents. The interfacial Nb–O distance distribution (Fig. S2) broadens and exhibits a higher fraction of elongated Nb–O bonds, reflecting locally distorted and partially undercoordinated $NbO_x$ units. Such coordination instability hampers the formation of stable interfacial bonding configurations with NCM and further contributes to the weakened adhesion at the cathode–coating interface. This observation suggests that excessive Mg-incorporation compromises interfacial bonding, likely due to the destabilization of the local coordination environment or the introduction of unfavorable structural distortions at the interface.

To further investigate the coating–electrolyte interface, additional first-principles calculations were performed by constructing model structures of $[Li_{1-2x}Mg_x]NbO_3$ ($Mg_x$-LNO) in contact with a sulfide-based solid electrolyte ($Li_6PS_5Cl_{0.5}Br_{0.5}$). As shown in Fig. 1c, it was verified that the adhesion energy of $Mg_{1/12}$-LNO with $Li_6PS_5Cl_{0.5}Br_{0.5}$ (LPSCB) was found to be −10.4049 eV, substantially higher than that of pristine LNO, indicating enhanced interfacial stability with the solid electrolyte as well. These findings indicate that application of $Mg_{1/12}$-LNO can reinforce interfacial adhesion at both the cathode–coating and coating–electrolyte interfaces compared to conventional LNO coating, thereby enhancing electrochemical performance and long-term cycling stability. Moreover, through the nudged elastic band (NEB) calculations, it was verified that $Mg_{1/12}$-LNO exhibited a significantly lower diffusion barrier (932.83 meV) compared to LNO (1331.81 meV) (Fig. 1d), indicating more facile $Li^+$ transport in $Mg_{1/12}$-LNO compared to LNO. In addition, pellet EIS measurements using blocking electrodes (Fig. S3) show that $Mg_{0.05}$-LNO exhibits a higher $Li^+$ ionic conductivity ($\sigma Li^+$) than pristine LNO, with $\sigma Li^+$ of ~$1.5 \times 10^{-7}$ S/cm for $Mg_{0.05}$-LNO

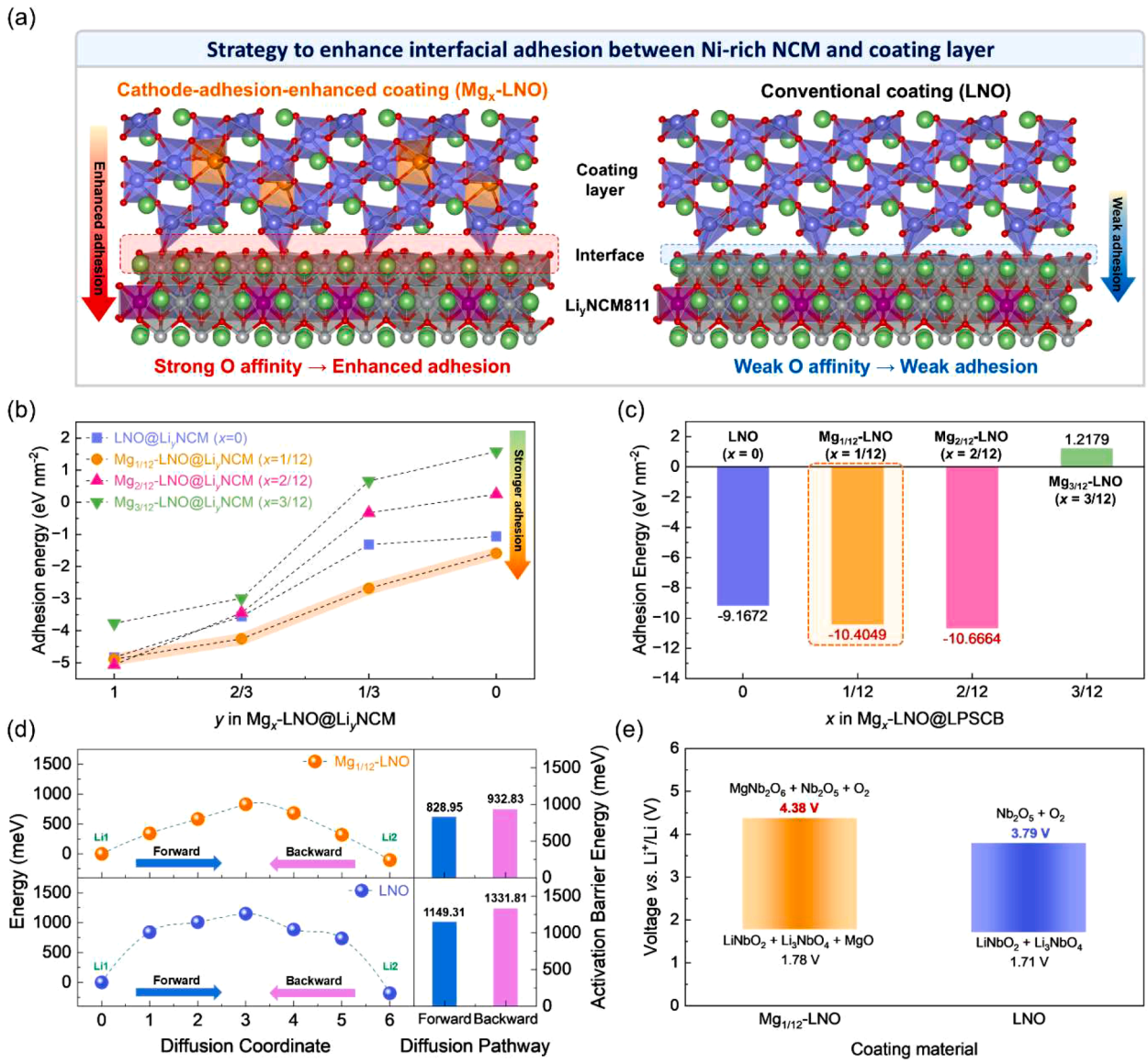


**Fig. 1.** First-principles calculation results comparing Mg$_x$-LNO and LNO coatings for Ni-rich NCM cathodes. (a) Schematic illustrating the interfacial contact between the Ni-rich NCM811 cathode and either cathode-adhesion-enhanced coating (Mg$_x$-LNO) or conventional coating (LNO). (b) Adhesion energies between Mg$_x$-LNO ($x$ = 0, 1/12, 2/12, 3/12) and Li$_y$NCM ($y$ = 1, 0.67, 0.33, 0) at various delithiated states. (c) Adhesion energies between Mg$_x$-LNO and sulfide solid electrolyte of LPSCB. (d) Predicted activation barrier energies for $Li^+$ ion diffusion in Mg$_{1/12}$-LNO and LNO structures. (e) Theoretical electrochemical stability windows of Mg$_{1/12}$-LNO and LNO.

compared to ~$9.7 \times 10^{-8}$ S/cm for LNO [57].

Notably, we verified that Mg$_{1/12}$-LNO possesses a wider electrochemical potential window than conventional LNO, particularly in the high-voltage region. The coating layer is susceptible to decomposition when exposed to the high-voltage environment, as well as to structural distortion and oxidation-state variation of the cathode during charge. For conventional LNO, the theoretical electrochemical stability window was calculated to range from 1.71 to 3.79 V. In contrast, Mg$_{1/12}$-LNO exhibits a significantly expanded window from 1.78 to 4.38 V (Fig. 1f). Consistent with this prediction, linear sweep voltammetry (LSV) measurements on pelletized bulk coating materials showed that Mg$_{0.05}$-LNO exhibits a lower oxidation current than pristine LNO up to 5.0 V, supporting the improved oxidative stability of CAEC (Fig. S4). The proposed cathode–adhesion-enhanced coating (CAEC), such as Mg$_{1/12}$-LNO, therefore offers not only stronger adhesion with the cathode but also superior stability under high-voltage conditions compared with conventional coatings (CCs). Consequently, CAEC-applied ASSBs are expected to deliver higher initial Coulombic efficiency (ICE) and maintain high energy density by suppressing voltage drop as well as capacity fading during prolonged cycling, compared to CC-applied ASSBs.

Mg$_{0.05}$-LNO was also experimentally confirmed to be synthesized with the same crystal structure as LNO without forming detectable impurity phases. Rietveld refinement of X-ray diffraction data (Fig. S5) confirmed that Mg$_{0.05}$-LNO retains a crystal structure analogous to that of pristine LNO, with no detectable impurity phases. Detailed structural information on atomic coordinates, occupancies, *etc*. are arranged in Table S2 and S3, indicating Mg-incorporation in the Li site. To further assess the crystallinity of coating material, we prepared highly crystalline Mg$_{0.05}$-LNO and LNO powders at elevated temperature and compared their XRD patterns with those obtained under the low-temperature conditions used for cathode coating (Fig. S6). While Mg$_{0.05}$-LNO and LNO synthesized in high-temperature exhibit sharp and intense diffraction peaks, the low-temperature products show substantially weakened and broadened features, indicating that the coating layers formed during the low-temperature coating process are low-crystallinity or near-amorphous. In addition, the electrochemical

performance was compared as a function of coating crystallinity. The high-crystalline sample was prepared at 600 °C as a representative crystallization condition for $LiNbO_3$-based coatings, while minimizing more severe interfacial reaction or thermal degradation of the cathode active material (Fig. S7) [58,59]. The electrochemical performances of the low-crystalline and high-crystalline CAEC were compared in Fig. S8. Compared with the high-crystalline coating, the low-crystalline or near-amorphous CAEC exhibited superior electrochemical performance, delivering a higher initial Coulombic efficiency and improved rate capability. These results suggest that the low-crystalline CAEC provides a more favorable interfacial environment for $Li^+$ transport than the highly crystalline coating [60,61]. A more detailed discussion of the coating crystallinity is presented in Fig. 5.

X-ray absorption near-edge spectroscopy (XANES) of the Nb K-edge (Fig. S9) indicated that the Nb ions in both LNO and $Mg_{0.05}$-LNO have the +5 oxidation state, confirming that Mg substitution does not alter the redox state of the host framework. These experimental results indicate that $Mg_{0.05}$-LNO can be applied as a CAEC.

### 3.2. Structural and morphological characterization of CAEC-NCM811 and CC-NCM811

$Mg_{0.05}$-LNO (as the CAEC) and LNO (as the CC) were applied to NCM811 cathode powders via a wet chemical process. To experimentally clarify the rationale for the optimal CAEC condition, CAEC-NCM811 cathodes with different coating loadings (0.5, 1, and 2 wt%) were prepared and evaluated under identical ASSB conditions. The 0.5 wt% sample exhibited inferior ICE and rate performance, attributable to incomplete surface coverage and increased parasitic interfacial reactions. Conversely, the 2 wt% sample showed reduced capacity across all tested current densities, indicating that excessive coating thickness introduces $Li^+$ transport limitations. Therefore, the 1 wt% CAEC condition was determined to be optimal, providing the most favorable balance between interfacial protection and $Li^+$ transport efficiency (Fig. S10 and S11). Fig. 2a shows the XRD patterns of 1wt% $Mg_{0.05}$-LNO-coated NCM811 (CAEC-NCM811), 1 wt% LNO-coated NCM811 (CC-NCM811), and bare NCM811 (B-NCM811), which indicate that the coating process did not introduce any noticeable structural changes and that the original NCM811 framework was well preserved. Rietveld refinement of X-ray diffraction (XRD) patterns for CAEC-NCM811 (Fig. 2b), CC-NCM811 and B-NCM811 (Fig. S12 and S13) confirmed that all three samples maintained the typical hexagonal layered structure with the $R\bar{3}m$ space group. The lattice parameters for CAEC-NCM811 were determined to be $a$ (= $b$) = 2.86714(6) Å and $c$ = 14.1673(7) Å, which are similar to those for CC-NCM811 and B-NCM811. Detailed structural information, including atomic positions and site occupancies for all three samples, are tabulated in Table S4–6. Notably, the refined cell parameters show only marginal variations

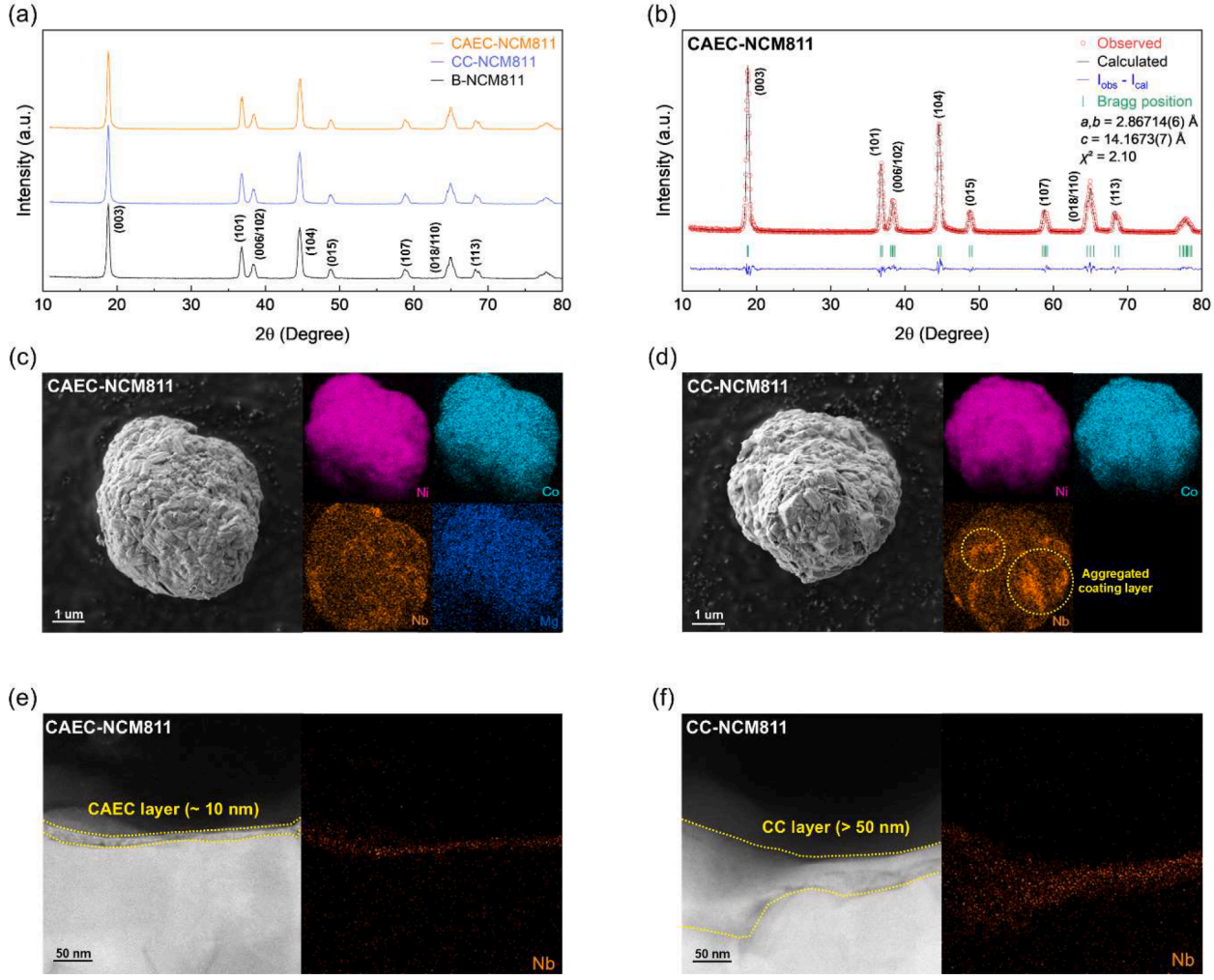


**Fig. 2.** Structural and morphological characterizations of CAEC—NCM811 and CC—NCM811. XRD patterns of $Mg_{0.05}$-LNO coated NCM (CAEC—NCM811), LNO-coated NCM811 (CC—NCM811), and bare NCM811 (B-NCM811) powders. Rietveld refinement results of XRD patterns for (b) CAEC—NCM811 powder. SEM image and corresponding elemental mapping of Nb, Mg, Ni, and Co by SEM-EDS at the particle level for (c) CAEC—NCM811 and (d) CC—NCM811. Cross-sectional HAADF-STEM images of the (e) CAEC—NCM811 and (f) CC—NCM811 samples, along with the corresponding EDS elemental mapping of Nb.

among B-, CC-, and CAEC-NCM811 (Tables S4–S6). Quantitatively, the refined lattice parameters show only marginal variations among the three samples (Tables S4–S6). B-NCM811 exhibits $a$ (= $b$) = 2.86731(6) Å, $c$ = 14.1747(7) Å (Table S4), CC-NCM811 shows $a$ (= $b$) = 2.86450(4) Å, $c$ = 14.1669(5) Å (Table S5) and CAEC-NCM811 shows $a$ (= $b$) = 2.86714(6) Å, $c$ = 14.1673(7) Å (Table S6), corresponding to $c/a$ ratios of 4.9436, 4.9457, and 4.9413, respectively. The maximum deviations are < 0.10% in $a$ and < 0.06% in $c$, indicating that the coating treatments do not measurably perturb the bulk layered lattice of NCM811. In terms of $Li^+$ transport, such small changes in $a$, $c$, and $c/a$ are not expected to significantly modify bulk $Li^+$ diffusion in the layered framework. Overall, these minor lattice-parameter variations suggest that the coatings do not alter the bulk framework, implying that the primary role of the coatings is associated with interfacial regulation rather than bulk structural modification.

Scanning electron microscopy (SEM) images (Fig. 2c-d) showed that both CAEC-NCM811 and CC-NCM811 maintained a spherical particle morphology with an average size of approximately 5 um. Their particle sizes were comparable to those of the B-NCM811 (Fig. S14). Interestingly, the degree of coating coverage on NCM811 particles differed markedly between CAEC and CC. As shown in Fig. 2c, elemental mapping using scanning electron microscopy–energy dispersive X-ray spectroscopy (SEM-EDS) revealed that, under the application of 1 wt% coating, Nb and Mg elements in CAEC-NCM811 were uniformly distributed across the surface of NCM811 particles alongside Ni and Co. SEM-EDS showed atomic ratios of CAEC-NCM811 were Ni = 25.09%, Co = 2.78%, Mn = 2.57%, Nb = 0.57%, Mg = 0.10%, and O = 68.90%. The presence and distribution of Nb and Mg on the coated surface were further confirmed by time-of-flight secondary ion mass spectrometry (ToF-SIMS) analysis (Fig. S15). In contrast, CC-NCM811 exhibited clear signs of aggregation under identical coating conditions (Fig. 2d), resulting in uneven coverage and partial exposure of the underlying NCM811 particles. Consistently, the SEM-EDS atomic ratios for CC-NCM811 were Ni = 22.93%, Co = 2.54%, Mn = 2.23%, Nb = 0.72%, and $O$ = 71.59%, indicating the presence of Nb but with less conformal distribution under the same coating loading. To more precisely quantify the coating-derived elemental composition, we additionally performed ICP–OES analysis on the coated cathode powders. The ICP–OES results, summarized in Tables S7 and S8, provide the measured elemental fractions of the coated materials, confirming the incorporation of Nb in both samples and the successful introduction of Mg in CAEC–NCM811. Notably, CAEC–NCM811 shows detectable Mg together with Nb, consistent with the intended $Mg_{0.05}$-LNO coating composition. These quantitative data complement the surface-sensitive SEM-EDS results and support the formation of the designed coating chemistry under the same 1 wt% coating condition.

As shown in the low-resolution, wide-area SEM-EDS mapping of Nb (Fig. S16), the CAEC forms a more homogeneous and continuous coating layer, whereas the CC shows Nb-rich domains, indicating poorer coating uniformity and lack of interfacial completeness. This distinction underscores the superior adhesion of the CAEC to the NCM811 surface, as evidenced by its more conformal and continuous coating layer. The improved interfacial contact offered by the CAEC is expected to enhance surface protection and contribute to greater interfacial stability during prolonged cycling.

Cross-sectional scanning high-angle annular dark-field transmission electron microscopy (HAADF-STEM) and STEM-EDS elemental mapping analyses, performed on focused ion beam (FIB)-processed samples, further confirmed that the coating layer on CAEC-NCM811 (Fig. 2e) was thinner (~ 10 nm) and more uniformly formed compared to that on CC-NCM811 (> 50 nm) (Fig. 2f), aligning well with the previously discussed first-principles calculation and SEM-EDS results. These observations clearly demonstrate that CAEC-NCM811 forms a thinner, more uniform, and better-adhered layer on the particle surface of NCM811, which effectively mitigates interfacial heterogeneity and provides a robust morphological foundation for improving the long-term stability of solid-state batteries.

### 3.3. Electrochemical properties of CAEC-applied ASSBs (CAEC@ASSBs) and CC-applied ASSBs (CC@ASSBs)

To comprehensively evaluate how CAEC can affect the electrochemical performance under the ASSB system, we systematically investigated the electrochemical behavior of CAEC-applied ASSB (CAEC@ASSB) and CC-applied ASSB (CC@ASSB) within a voltage range of 2.5–4.25 V. Electrochemical tests of the ASSBs were conducted using a pressurization-type cell configuration of composite cathode ‖ $Li_6PS_5Cl_{0.5}Br_{0.5}$ ‖ Li metal, employing Li metal anode to create a stringent environment that challenges interfacial stability under high energy density conditions [62,63]. Furthermore, to demonstrate the feasibility of practical-level electrode architectures, a high-loading cathode featuring ~15 mg $cm^{-2}$ of active material and a thickness of ~180 um was employed. Detailed experimental procedures, including cell assembly and measurement protocols, are provided in the Experimental Section. The sulfide-based solid electrolyte, $Li_6PS_5Cl_{0.5}Br_{0.5}$, exhibited an ionic conductivity of approximately 4.5 mS $cm^{-1}$ at room temperature (Fig. S17), and its single-phase argyrodite structure was confirmed by XRD measurement (Fig. S18) [64].

Fig. 3a-b present the first-cycle charge–discharge profiles of the two cathodes. At a current density of C/10 (1C = 185 mA $g^{-1}$), the CAEC@ASSB delivered an initial charge capacity of 220.59 mAh $g^{-1}$ and a discharge capacity of 202.30 mAh $g^{-1}$, achieving an initial Coulombic efficiency (ICE) of 91.7%. In comparison, the CC@ASSB exhibited an initial charge and discharge capacity of 217.83 and 195.99 mAh $g^{-1}$, respectively, corresponding to an ICE of 90.4%. This enhanced electrochemical reversibility under the ASSB system is attributed to the improved cathode–coating interfacial adhesion through application of the CAEC, which in turn facilitates more stable interfacial ion transport. Consistently, electrochemical impedance spectroscopy (EIS) analysis of fresh cells (Fig. S19) further supported this interpretation. CAEC@ASSB exhibited a lower charge transfer resistance ($R_{ct}$) of 34.8 Ω compared to 45.0 Ω for CC@ASSB, reflecting more efficient Li-ion transport across the cathode–coating–electrolyte interfaces. Moreover, to probe growth of SCL-like interfacial polarization under purely contact-driven conditions, we prepared unbiased composite pellets by mixing coated NCM811 with $Li_6PS_5Cl_{0.5}Br_{0.5}$ at a 1:1 v/v% and measured EIS at 0 h and after 48 h of static contact (Fig. S20). Both composites show impedance growth, but CAEC-NCM811 exhibits markedly smaller increases ($\Delta R_b$ = 0.3 Ω, $\Delta R_{total}$ = 6.7 Ω) than CC-NCM811 ($\Delta R_b$ = 1.6 Ω, $\Delta R_{total}$ = 7.6 Ω), indicating suppressed contact-induced polarization development. This tendency is consistent with the wider electrochemical stability window and improved coating conformity and coverage enabled by stronger adhesion, which mitigates pArasitic interfacial resistance and heterogeneous potential drops at the cathode and S-SE interface.

The beneficial effects of improved adhesion and enhanced $Li^+$ transport were further validated by rate capability tests. At a high current density of 2C, the CAEC@ASSB delivered 146.78 mAh $g^{-1}$, corresponding to 73.4% of its C/10 capacity, whereas CC@ASSB retained only 71.5% under the same condition, demonstrating superior high-rate utilization by CAEC (Fig. 3c-d). Furthermore, the CAEC@ASSB maintained stable capacity retention across repeated cycles under varying current densities, while the CC@ASSB exhibited irreversible capacity fading, indicative of progressive interfacial degradation (Fig. S21). Moreover, to validate these results, we conducted a Galvanostatic Intermittent Titration Technique (GITT) test, as originally introduced by Weppner and Huggins [65,66]. The average $Li^+$ diffusion coefficient of the CAEC@ASSB was calculated to be $1.323 \times 10^{-8}$ $cm^2$ $s^{-1}$, which is slightly higher than that of the CC@ASSB ($1.266 \times 10^{-8}$ $cm^2$ $s^{-1}$), indicating enhanced ionic transport kinetics (Fig. S22).

In the ASSB system, the improvement in long-term cycling performance resulting from the application of the CAEC is prominently observed. After 100 cycles, the CAEC@ASSB retained 81.0% of its initial

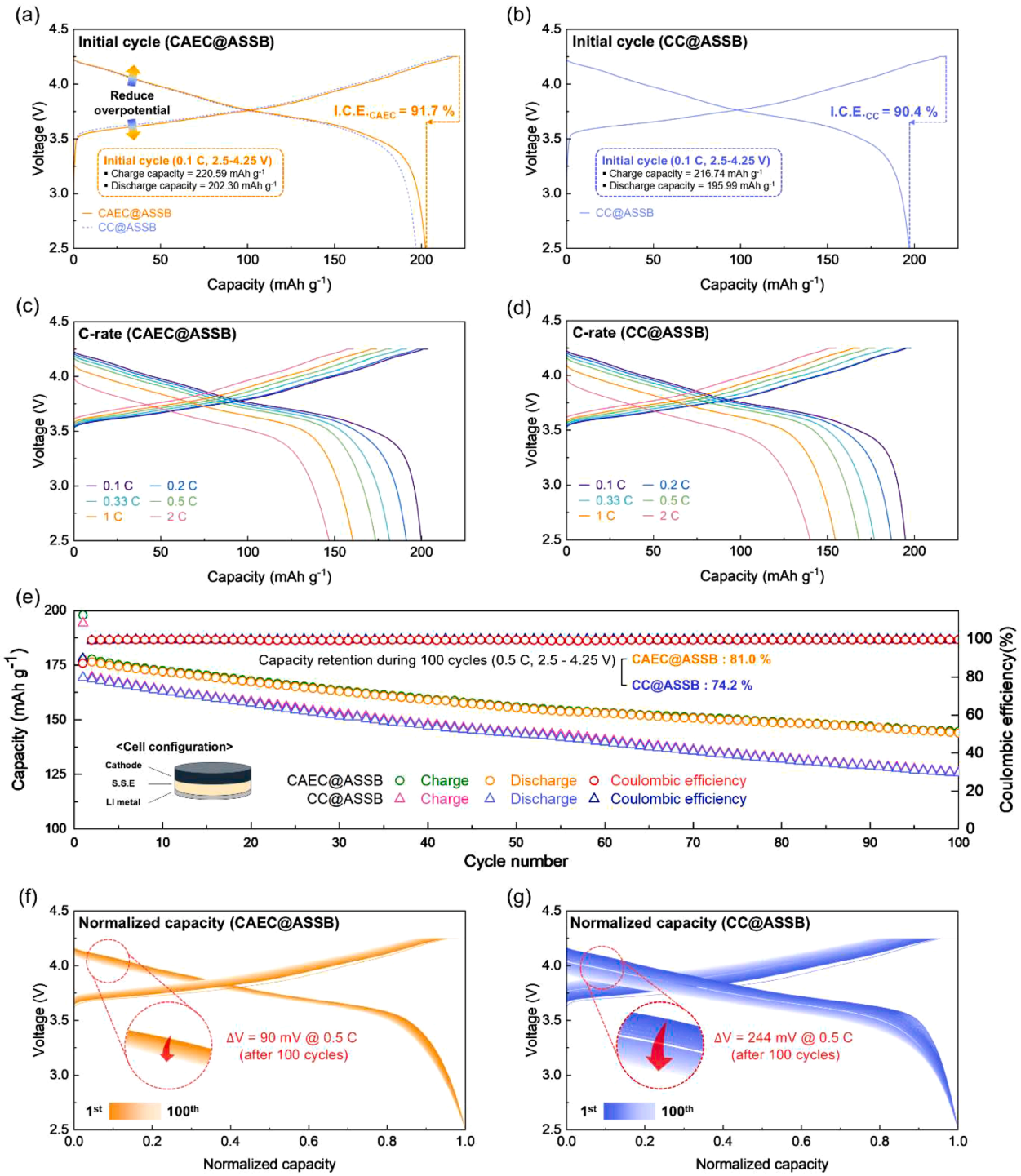


**Fig. 3.** Comparison of the electrochemical properties of CAEC@ASSB and CC@ASSB. Initial charge and discharge profiles of (a) CAEC-applied ASSB (CAEC@ASSB), orange) and (b) CC-applied ASSB (CC@ASSB, blue) in the voltage range of 2.5–4.25 V (vs. $Li^+$/Li) at current density of C/10. Charge and discharge curves of (c) CAEC@ASSB and (d) CC@ASSB in the voltage range of 2.5–4.25 V (vs. $Li^+$/Li) measured at various discharging current densities with a constant charge current density of C/10. (e) Cycle performances of CAEC@ASSB and CC@ASSB at current density of C/2 over 100 cycles in the voltage range of 2.5–4.25 V (vs. $Li^+$/Li) including schematic of the cell configuration (Li metal ‖ $Li_6PS_5Cl_{0.5}Br_{0.5}$ ‖ composite cathode) used for electrochemical evaluation. Comparison of normalized charge/discharge profiles for (f) CAEC@ASSB and (g) CC@ASSB over 100 cycles at 0.5C, highlighting the evolution of polarization.

capacity with a Coulombic efficiency exceeding 99.5%, whereas the CC@ASSB showed a capacity retention of 74.2% (Fig. 3e). The non-coating-based ASSB (N-C@ASSB), by comparison, retained only 69.1% of its initial capacity under identical conditions (Fig. S23), highlighting the protective effect of the CAEC against degradation induced by the sulfide-based solid electrolyte. Furthermore, the normalized charge/discharge profiles of the CAEC@ASSB and the CC@ASSB demonstrate distinct differences in cycling performance, particularly in the evolution of voltage polarization (Fig. 3f-g) [2,4,67]. After 100 cycles at 0.5C, the CAEC@ASSB exhibited a markedly lower polarization of 90 mV compared to 244 mV for the CC@ASSB, indicating suppressed parasitic resistance likely arising from interfacial side reactions. Consistently, post-cycling EIS after 100 cycles shows that CAEC@ASSB retains a lower total impedance than CC@ASSB (Fig. S24), supporting the reduced

voltage polarization of CAEC@ASSB.

Furthermore, the differential capacity versus voltage (dQ/dV) profiles after 100 cycles further support the superior electrochemical stability of the CAEC@ASSB. As shown in Fig. S25, the CAEC@ASSB maintained sharp and well-defined redox peaks even after prolonged cycling, indicating preserved reaction kinetics and minimal polarization growth [2,4,67]. In contrast, the CC@ASSB exhibited a noticeable broadening and shift of redox peaks, suggesting increased interfacial resistance and sluggish $Li^+$ transport upon cycling. These observations are consistent with the observed capacity retention trend and further confirm the stabilizing effect of the CAEC at the cathode–electrolyte interface. Furthermore, the CAEC@ASSB demonstrated superior

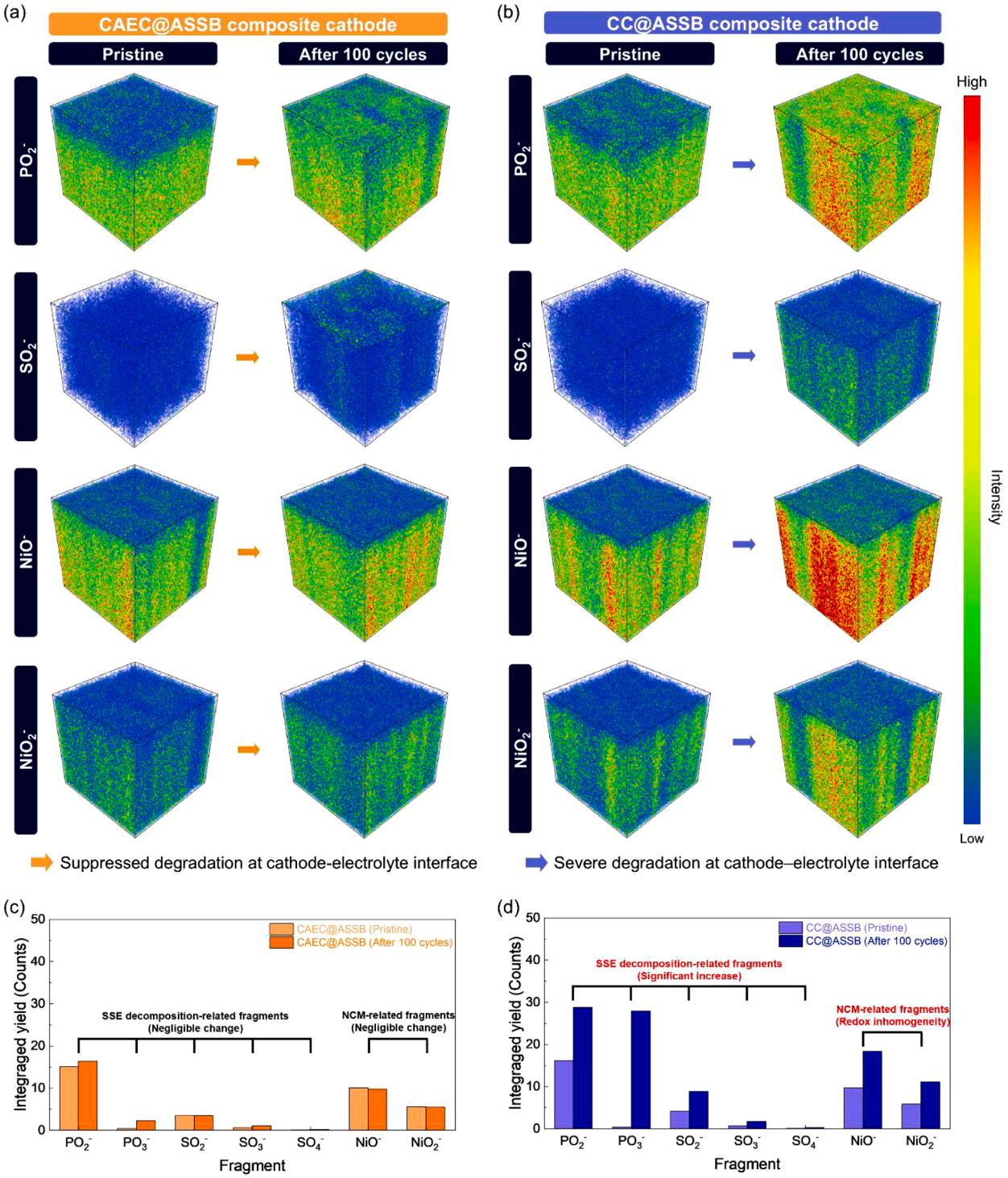


**Fig. 4.** Interfacial degradation in CAEC—NCM811 and CC—NCM811 composite cathodes revealed by ToF-SIMS. Negative ion ToF-SIMS 3D mappings were conducted for CAEC@ASSB and CC@ASSB composite cathodes in both pristine and 100-cycled states. The electrodes were cycled 100 times in the voltage range of 2.5–4.25 V (vs. $Li^+$/Li) at a current density of C/2. (a) ToF-SIMS 3D mappings of $PO_2^-$, $SO_2^-$, $NiO^-$, and $NiO_2^-$ in CAEC@ASSB composite cathodes. (b) Corresponding ToF-SIMS mappings in CC@ASSB composite cathodes. Quantitative comparison of the integrated negative-ion yields obtained from normalized depth profiles for representative sulfide based solid electrolyte (S-SE)-related fragments ($PO_x^-$, $SO_x^-$) and NCM811-related fragments ($NiO_x^-$) in (c) CAEC@ASSB and (d) CC@ASSB composite cathode, comparing pristine and 100 cycled states.

capacity retention (83.7%) even at a high cut-off voltage of 4.35 V, outperforming the CC@ASSB (76.5%) under the same conditions (Fig. S26). This result is consistent with the broader electrochemical stability window predicted for the CAEC by theoretical calculations. To further assess the practical significance of the present electrochemical performance, we compared our results with recently reported sulfide-based all-solid-state batteries using Ni-rich layered cathodes, as summarized in Table S11 [68–71]. As the reported electrochemical performances depend on various experimental parameters, including anode type, cathode loading, operating voltage window, and applied current density, a meaningful comparison requires careful consideration of these differences. In this context, the present cell was evaluated under relatively stringent conditions, including the use of Li metal anode and a high cathode loading ($\geq$ 15 mg cm$^{-2}$). Despite these demanding conditions, the CAEC-based cathode delivers high initial capacity and maintains cycling performance comparable to those reported in the literature, highlighting its effectiveness under practically relevant conditions.

### 3.4. Interfacial stability and surface degradation behavior in CAEC-applied ASSBs (CAEC@ASSBs)

To further verify the origins of the enhanced electrochemical performance, particularly regarding interfacial stability, we investigated the chemical degradation behavior at the cathode–electrolyte interface using time-of-flight secondary ion mass spectrometry (ToF-SIMS) analysis. This analysis was employed to qualitatively and semi-quantitatively assess the by-products generated through chemical decomposition, which are critical contributors to increased interfacial resistance. Given the strong reactivity of oxygen with phosphorus and sulfur, phosphate ($PO_x^-$) and sulfite/sulfate ($SO_x^-$) fragments were considered key indicators of oxygen-driven interfacial degradation. Additionally, the presence of $NiO^-$ and $NiO_2^-$, resulting from the oxidation of nickel species, served as a marker of oxygen-induced structural deterioration in the cathode material [45,46].

Three-dimensional (3D) ToF-SIMS mappings revealed the distribution of chemical species in the pristine and electrochemically cycled composite cathodes composed of the CAEC@ASSB and the CC@ASSB, mixed with $Li_6PS_5Cl_{0.5}Br_{0.5}$ solid electrolyte and Super C65 conductive additive. Before cycling, as shown in Fig. 4a-b, both cathodes exhibited comparable intensities of sulfur ($SO_2^-$), phosphorus ($PO_2^-$), and nickel ($NiO^-$ and $NiO_2^-$) related species. However, after 100 cycles at a current density of 0.5C, the CC@ASSB showed pronounced accumulation of degradation by-products, arising from oxygen-driven side reactions of the sulfide-based solid electrolyte and from the degradation of the Ni-rich NCM cathode (Fig. 4b). This observation suggests that the CC was not chemically stable under prolonged cycling, and its decomposition products participated in undesirable side reactions with the sulfide electrolyte, accelerating the formation of interfacial degradation species. In contrast, the CAEC@ASSB exhibited substantially suppressed intensities of oxygen-induced degradation fragments such as sulfur- and phosphorus-related species, indicating a more stable cathode-electrolyte interface (Fig. 4a).

These observations were further corroborated by ToF-SIMS depth-profile analyses (Fig. S27), where the sputter-depth axis spans the entire cathode-electrolyte composite, simultaneously covering the surface coating/interphase region near the particle exterior, the bulk cathode, and the SSE-containing region. Based on the depth-profiles results, we conducted a semi-quantitative comparison by integrating the fragment yields of $PO_x^-$, $SO_x^-$, and $NiO_x^-$ within each regime and comparing CAEC@ASSB and CC@ASSB (Fig. 4c-d, Table S9 and Table S10). After 100 cycles, CC@ASSB shows a pronounced increase of $PO_x^-$ and $SO_x^-$ signals and their extended presence toward deeper regions, indicating severe oxygen-driven interfacial degradation and progressive interphase growth. In addition, the $NiO^-$ and $NiO_2^-$ signals exhibit a more distinct increase in CC@ASSB near the cathode-side region, consistent with enhanced surface reconstruction/oxidation and contact deterioration upon cycling (Fig. 4d). In contrast, CAEC@ASSB displays only minor changes in the integrated $PO_x^-$ and $SO_x^-$ yields across the corresponding regions, and $NiO_x^-$ signals remain comparatively stable, supporting suppressed interfacial degradation and preserved cathode integrity (Fig. 4c).

Importantly, this improvement in interfacial stability is not merely a result of intrinsic chemical inertness but is closely linked to the enhanced cathode–coating interfacial adhesion achieved through application of the CAEC. The strengthened adhesion promotes more conformal and continuous coating coverage, which reduces locally exposed cathode areas that can directly react with the sulfide electrolyte. Consequently, CAEC more effectively mitigates oxygen-driven side reactions and the formation of ion-blocking interphase species, thereby preserving interface integrity during prolonged cycling.

In addition to the improved chemical stability at the cathode–electrolyte interface, the CAEC also contributed to enhanced structural stability of NCM811 cathode during electrochemical cycling under the ASSB system. As shown in Fig. 5a-b, *ex-situ* XRD analysis of the composite electrodes at various electrochemical states revealed distinct trends in structural evolution. Notably, CAEC-NCM811 and CC-NCM811 exhibited markedly different peak shifts, broadening, and intensity changes during charge and discharge processes over 100 cycles. In particular, Fig. 5c highlights the evolution of the (003) reflection, a sensitive indicator of *c*-axis lattice changes in layered oxides. CAEC-NCM811 exhibited a smaller peak shift ($\Delta 2\theta \approx 0.101^\circ$) and maintained high peak intensity even after 100 cycles, suggesting minimal structural distortion and sustained crystallinity. In contrast, CC-NCM811 showed a greater shift ($\Delta 2\theta \approx 0.140^\circ$) along with noticeable peak broadening and intensity loss, which are typically associated with microcracking, contact loss, or degradation of the layered structure [44, 72,73]. These structural differences were further quantified in Fig. 5d, where the evolution of the *c*-lattice parameter was tracked across three electrochemical states. The total variation in *c*-lattice from pristine to the 100th discharge state ($\Delta c$-lattice) was smaller in CAEC-NCM811 (0.43%) than in CC-NCM811 (0.70%). This suppressed lattice fluctuation directly correlates with reduced mechanical stress and better structural stability.

To more quantitatively evaluate lattice-strain evolution and its linkage to cycling-induced mechanical stress, we performed Williamson–Hall (W–H) analysis on the ex-situ XRD patterns of the composite cathodes using the (003), (101), and (104) reflections (Fig. 5a-b and Fig. S28). The detailed fitting parameters are summarized in Table S12–S17, and the extracted microstrain (ε) values are plotted in Fig. S29. Among the three samples, CAEC-NCM811 exhibits the most stable microstrain behavior upon cycling, showing only a ~3% increase relative to the pristine state after 100 cycles. In contrast, CC-NCM811 displays a ~21% increase in microstrain, whereas bare B-NCM811 undergoes severe strain accumulation with an increase of ~102% compared to its initial value. These results, together with the suppressed c-lattice fluctuation and reduced intra-particle cracking for CAEC-NCM811 after 100 cycles (Fig. S30), indicate that CAEC more effectively mitigates cycling-induced stress accumulation and better preserves particle integrity and interfacial contact than CC. Such improved mechanical stability is expected to suppress contact loss within the composite cathode and maintain continuous ionic and electronic percolation pathways during cycling, thereby mitigating localized electronic isolation and irreversible side reactions. AFM-based modulus measurements indicate that CAEC-NCM811 exhibits the highest mechanical stiffness among the three cathodes, suggesting enhanced resistance to cycling-induced deformation (Table S18). Consistently, nanoindentation results confirm that CAEC-NCM811 exhibits the highest hardness and reduced modulus among the compared samples in the pristine state (Table S19). More importantly, CAEC-NCM811 shows a substantially higher reduced modulus after cycling, whereas CC-NCM811 shows more pronounced mechanical degradation, indicating

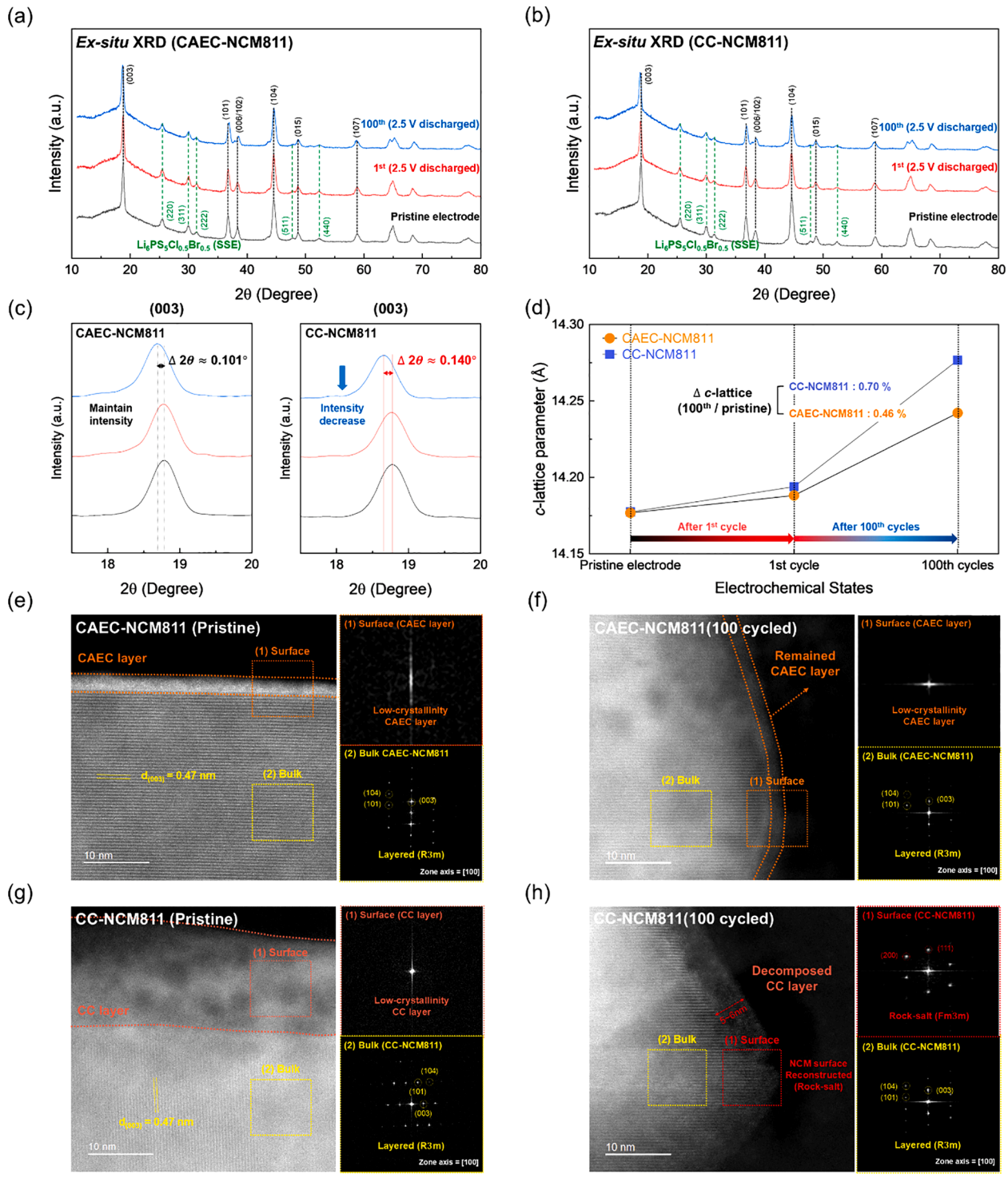


**Fig. 5.** Structural stability and surface evolution of CAEC—NCM811 and CC—NCM811 upon electrochemical cycling. *Ex-situ* XRD patterns of (a) CAEC–NCM811 and (b) CC–NCM811 collected at the pristine state, after the 1st discharge (2.5 V), and after the 100th discharge (2.5 V). (c) Enlarged views of the (003) reflections showing a smaller peak shift and maintained intensity in CAEC—NCM811 (left), whereas CC—NCM811 exhibits a larger peak shift and pronounced intensity reduction (right), indicative of structural degradation. (d) Evolution of *c*-lattice parameters calculated from the (003) reflection during 100 cycles, revealing a smaller lattice change in CAEC—NCM811 compared with CC—NCM811. High-resolution scanning transmission electron microscopy (HR-STEM) images and the corresponding FFT analyses of CAEC—NCM811 in (e) pristine state and (f) after 100 cycles. HR-STEM images and the corresponding FFT analyses of CC—NCM811 in (g) the pristine state and (h) after 100 cycles.

superior mechanical stability of the CAEC under repeated electrochemical cycling (Table S20 and S21). This behavior is further supported by DFT calculations, which show that CAEC-NCM811 undergoes a smaller change in local *c*-axis interlayer spacing during delithiation than CC-NCM811, suggesting suppressed structural disorder and local stress accumulation at the cathode surface (Fig. S31). These results support our conclusion that the CAEC strategy improves mechanical stability, which is expected to suppress contact loss within the cathode composite and maintain continuous ionic or electronic percolation pathways during cycling, thereby mitigating localized electronic isolation and

irreversible side reactions. Supporting this interpretation, ToF-SIMS analysis (Fig. 4a-b) shows a markedly higher accumulation of Ni-related fragments in CC@ASSB, consistent with irreversible Ni redox processes promoted by contact deterioration and electronic isolation. In contrast, CAEC@ASSB exhibits lower $NiO^-$ and $NiO_2^-$ intensities, in line with improved contact retention and mitigated mechanical failure.

To evaluate the long-term stability of the coating layers and NCM811 cathodes, post-cycle HR-STEM analyses were performed after 100 cycles together with STEM-EDS mapping. As shown in Fig. 5e–h, HR-STEM images and the corresponding FFT analyses are provided for both the pristine and after 100 cycles, enabling a direct comparison of the surface structure evolution. In CAEC-NCM811, a surface structure remains discernible after cycling and the near-surface FFT retains a layered $R\bar{3}m$ structure (Fig. 5e–f), indicating suppressed surface reconstruction. Notably, the CAEC-NCM811 appears as a thin, conformal, and continuous surface region in the pristine state (Fig. 5e), and this interfacial layer remains visually defined after cycling (Fig. 5f), consistent with electrochemical stability of CAEC. Consistently, STEM-EDS mapping of CAEC-NCM811 shows a thin and uniform Nb-enriched surface region in the pristine state (Fig. S32) and, importantly, the Nb-containing surface layer remains clearly detectable even after cycling (Fig. S33), supporting retention of the CAEC coating at the cathode surface. This persistence of the Nb-containing layer after prolonged cycling further indicates the electrochemical robustness of CAEC, its higher stability against decomposition under operating potentials, thereby enabling sustained interfacial protection. In contrast, CC-NCM811 shows clear evidence of coating degradation after cycling. While a distinct Nb-enriched surface layer is observed in the pristine state (Fig. S34), the coating layer becomes hardly discernible after cycling, and the coating-layer contrast becomes obscured with Nb appearing broadly distributed (Fig. S35), consistent with partial decomposition of the CC. In agreement, the near-surface FFT after cycling exhibits features consistent with a cubic rock-salt-like phase ($Fm\bar{3}m$) (Fig. 5h), indicating pronounced surface reconstruction. Furthermore, X-ray photoelectron spectroscopy (XPS) analyses of the Nb 3*d* and Mg 2*p* regions showed that the CAEC chemistry was largely preserved after cycling, whereas the CC sample exhibited noticeable change in Nb 3*d* spectral intensity, indicating weaker interfacial stability (Fig. S36 and S37) [74,75]. Collectively, these observations, together with the schematic illustration in Fig. 6, indicate that the CAEC forms a homogeneous and strongly adhered coating layer that preserves intimate contact between the cathode and the sulfide electrolyte during repeated (de)lithiation. Unlike the $LiNbO_3$-based CCs, which can suffer from non-uniform coverage and progressive interfacial separation upon cycling, the CAEC maintains a more conformal interface, thereby mitigating contact loss and local current constriction. In addition to its enhanced interfacial adhesion, the CAEC also exhibits improved mechanical robustness, as evidenced by the higher Young's modulus and hardness and the reduced microcrack formation after cycling. Moreover, by combining a wider electrochemical stability window with more facile $Li^+$ transport, the CAEC effectively suppresses parasitic interfacial reactions and reduces the accumulation of decomposition products at the cathode–electrolyte interface. As a result, the CAEC stabilizes the electrolyte–coating–cathode contact and maintains structural integrity of the interphase and near-surface cathode region, which collectively facilitates continuous $Li^+$ transport pathways, lowers polarization growth, and preserves electrochemical reversibility over prolonged cycling. These results indicate that the beneficial effect of CAEC arises from the combined contributions of enhanced interfacial adhesion, improved mechanical robustness, superior electrochemical stability [25,44].

These beneficial effects are not limited to NCM811. To verify the broader applicability of the CAEC strategy, it was also applied to NCM955. XRD analysis confirmed preservation of the bulk crystal structure, while electrochemical tests showed improved cyclability and rate capability over bare NCM955 (Fig. S38 and S39). These results confirm that the proposed CAEC strategy is broadly applicable to Ni-rich layered cathodes beyond NCM811.

## 4. Conclusion

In summary, this study establishes a comprehensive understanding of how cathode–adhesion-enhanced coatings (CAECs) fundamentally improve interfacial stability and electrochemical performance in sulfide-based all-solid-state batteries (ASSBs). The CAEC strengthens bonding interactions and oxygen affinity within the crystal structure of a conventional coating (CC), $LiNbO_3$, thereby reinforcing interfacial adhesion and suppressing interfacial decomposition at the cathode–electrolyte boundary. Moreover, CAEC provides a lower activation barrier for $Li^+$

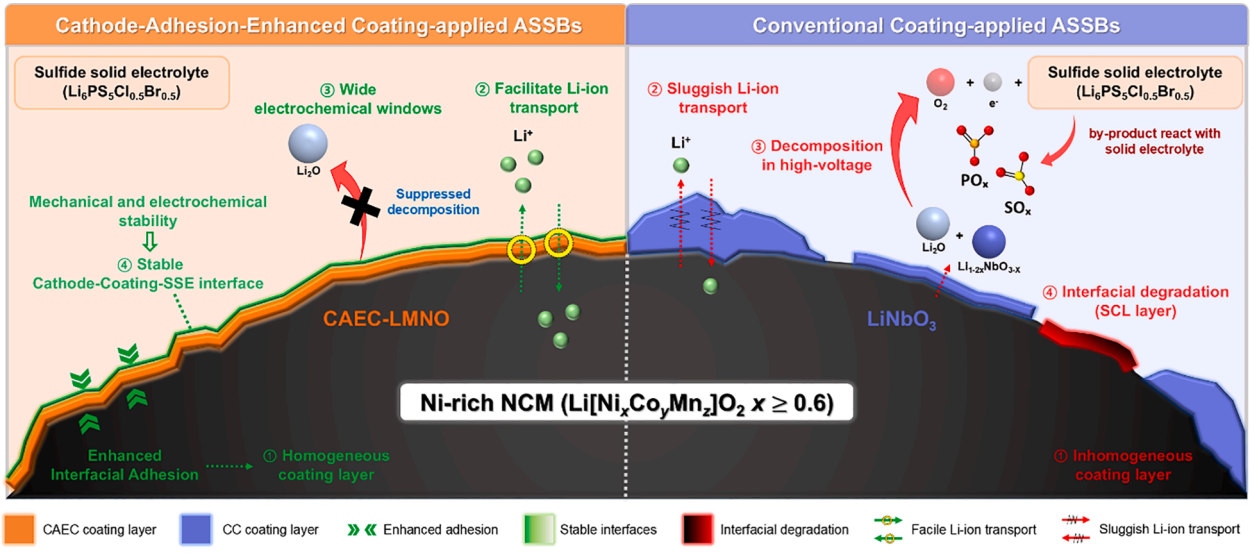


**Fig. 6.** Schematic comparison of cathode-adhesion-enhanced coating (CAEC, $Mg_{0.05}$-LNO) and conventional coating (CC, $LiNbO_3$) in sulfide-based all-solid-state batteries. The CAEC (left) forms a homogeneous and conformal coating through enhanced interfacial adhesion, facilitating $Li^+$ transport, and suppressing decomposition owing to the widened electrochemical stability window. In contrast, conventional coating (right) with weaker adhesion to Ni-rich cathodes can lead to inhomogeneous coverage, sluggish $Li^+$ diffusion, and severe interfacial degradation under high-voltage operation. CAEC strategy is expected to be generally applicable to other Ni-rich layered cathodes ($Li[Ni_xCo_yMn_z]O_2$, $x \geq 0.6$, $x + y + z = 1$).

transport and a wider electrochemical potential window than CC, enabling superior cycling stability, enhanced rate capability, and reliable operation under high-voltage conditions, as confirmed through integrated first-principles calculations and experimental analyses. Electrochemical evaluations further demonstrate that the CAEC@ASSB delivers a high initial discharge capacity of 202.30 mAh $g^{-1}$ and an initial Coulombic efficiency of 91.7%, both of which are higher than those of the CC@ASSB (195.99 mAh $g^{-1}$ and 90.4%). Notably, under a high cut-off voltage of 4.35 V, the CAEC@ASSB maintains 83.7% of its capacity after 50 cycles, outperforming CC@ASSB (76.5%). *Ex-situ* ToF-SIMS and XRD analyses further verify that the introduction of CAEC effectively suppresses interfacial decomposition and mitigates structural distortion of the NCM811 cathode during charge/discharge, thereby stably maintaining the crystal structure of the cathode after prolonged cycling under the ASSB system. These multi-scale characterizations provide mechanistic insight into how the CAEC mitigates interfacial degradation and structural evolution across different length scales, bridging atomistic bonding modulation with device-level stability. These findings highlight that the strengthened cathode–coating adhesion plays a crucial role in suppressing side reactions with the sulfide electrolyte, thereby stabilizing the cathode–electrolyte interface and enhancing the long-term electrochemical durability of the ASSB system. We believe that this strategy not only advances the understanding of interfacial chemistry–driven performance enhancement in all-solid-state batteries but also provides valuable insights for their practical implementation.

## CRediT authorship contribution statement

**Junseong Kim:** Writing – original draft, Visualization, Validation, Investigation, Formal analysis. **Hoseok Lee:** Writing – original draft, Visualization, Validation, Software, Formal analysis. **Taegyu Kim:** Methodology, Investigation. **Eunyoung Ryu:** Visualization, Methodology. **Imsul Seo:** Validation, Methodology. **Ju Yeong Seong:** Investigation, Formal analysis. **Chungbum Lim:** Validation, Investigation. **Jongsoon Kim:** Writing – review & editing, Visualization, Validation, Supervision, Project administration, Funding acquisition, Formal analysis, Data curation, Conceptualization.

## Declaration of competing interest

The authors declare the following financial interests/personal relationships which may be considered as potential competing interests:

Jongsoon Kim reports financial support was provided by Hyundai Motor Company. If there are other authors, they declare that they have no known competing financial interests or personal relationships that could have appeared to influence the work reported in this paper.

## Acknowledgments

This work was supported by HMC, Hyundai Motors Company, Ltd. Also, this work was supported by the National R&D Program through the National Research Foundation of Korea (NRF) funded by Ministry of Science and ICT (RS-2024-00408156) of Republic of Korea.

## Supplementary materials

Supplementary material associated with this article can be found, in the online version, at doi:10.1016/j.ensm.2026.105167.

## Data availability

Data will be made available on request.

## References

[1] J.B. Goodenough, K.S. Park, The Li-ion rechargeable battery: a perspective, J. Am. Chem. Soc. 135 (2013) 1167–1176, https://doi.org/10.1021/ja3091438.
[2] J. Kim, H. Ahn, J. Ahn, H. Park, J. Hong, M. Hwan Lee, H. Park, J. Kim, Activation of oxygen redox by inhibited dynamic phase transition for high-energy Li-rich layered oxide cathode, Chem. Eng. J. 495 (2024) 153122, https://doi.org/10.1016/j.cej.2024.153122.
[3] M. Choi, H. Choi, S. Park, W.M. Seong, Y. Lee, W. Ko, M. kyung Cho, J. Ahn, Y. Kong, J. Kim, Stabilized high-voltage operation of Co-free NMX cathode via CEI-controlling, Energy Storage Mater. 67 (2024) 103291, https://doi.org/10.1016/j.ensm.2024.103291.
[4] M. Choi, H.B. Lee, Y. Lee, H. Kweon, J. Ahn, B. Ku, J. Lee, S. Lee, J. Park, Y.M. Kim, J. Kim, Improving cyclability and structural stability of Co-free layered cathode by controlling porosity and cracks in secondary particles for low-cost and high-energy LIBs, Adv. Funct. Mater. 2424880 (2025) 1–15, https://doi.org/10.1002/adfm.202424880.
[5] V. Etacheri, R. Marom, R. Elazari, G. Salitra, D. Aurbach, Challenges in the development of advanced Li-ion batteries: a review, Energy Environ. Sci. 4 (2011) 3243, https://doi.org/10.1039/c1ee01598b.
[6] Q. Wang, P. Ping, X. Zhao, G. Chu, J. Sun, C. Chen, Thermal runaway caused fire and explosion of lithium ion battery, J. Power Sources. 208 (2012) 210–224, https://doi.org/10.1016/j.jpowsour.2012.02.038.
[7] X. Liu, D. Ren, H. Hsu, X. Feng, G.L. Xu, M. Zhuang, H. Gao, L. Lu, X. Han, Z. Chu, J. Li, X. He, K. Amine, M. Ouyang, Thermal runaway of lithium-ion batteries without internal short circuit, Joule 2 (2018) 2047–2064, https://doi.org/10.1016/j.joule.2018.06.015.
[8] M. Armand, Nature lithium battery, Nature 414 (2001) 359–367. http://www.ncbi.nlm.nih.gov/pubmed/11713543.
[9] A. Banerjee, X. Wang, C. Fang, E.A. Wu, Y.S. Meng, Interfaces and interphases in all-solid-State batteries with inorganic solid electrolytes, Chem. Rev. 120 (2020) 6878–6933, https://doi.org/10.1021/acs.chemrev.0c00101.
[10] S. Randau, D.A. Weber, O. Kötz, R. Koerver, P. Braun, A. Weber, E. Ivers-Tiffée, T. Adermann, J. Kulisch, W.G. Zeier, F.H. Richter, J. Janek, Benchmarking the performance of all-solid-state lithium batteries, Nat. Energy. 5 (2020) 259–270, https://doi.org/10.1038/s41560-020-0565-1.
[11] R. Schmuch, R. Wagner, G. Hörpel, T. Placke, M. Winter, Performance and cost of materials for lithium-based rechargeable automotive batteries, Nat. Energy. 3 (2018) 267–278, https://doi.org/10.1038/s41560-018-0107-2.
[12] J. Janek, W.G. Zeier, A solid future for battery development, Nat. Energy. 1 (2016) 1–4, https://doi.org/10.1038/nenergy.2016.141.
[13] S. Wang, Y. Wu, T. Ma, L. Chen, H. Li, F. Wu, Thermal stability between sulfide solid electrolytes and oxide cathode, ACS Nano 16 (2022) 16158–16176, https://doi.org/10.1021/acsnano.2c04905.
[14] P. Albertus, V. Anandan, C. Ban, N. Balsara, I. Belharouak, J. Buettner-Garrett, Z. Chen, C. Daniel, M. Doeff, N.J. Dudney, B. Dunn, S.J. Harris, S. Herle, E. Herbert, S. Kalnaus, J.A. Libera, D. Lu, S. Martin, B.D. McCloskey, M.T. McDowell, Y. S. Meng, J. Nanda, J. Sakamoto, E.C. Self, S. Tepavcevic, E. Wachsman, C. Wang, A. S. Westover, J. Xiao, T. Yersak, Challenges for and pathways toward Li-metal-based all-solid-State batteries, ACS Energy Lett. 6 (2021) 1399–1404, https://doi.org/10.1021/acsenergylett.1c00445.
[15] D. Cao, X. Sun, Y. Wang, H. Zhu, Bipolar stackings high voltage and high cell level energy density sulfide based all-solid-state batteries, Energ. Storage Mater. 48 (2022) 458–465, https://doi.org/10.1016/j.ensm.2022.03.012.
[16] C. Yu, L. Van Eijck, S. Ganapathy, M. Wagemaker, Synthesis, structure and electrochemical performance of the argyrodite Li6PS5Cl solid electrolyte for Li-ion solid state batteries, Electrochim. Acta. 215 (2016) 93–99, https://doi.org/10.1016/j.electacta.2016.08.081.
[17] H.J. Shin, J.T. Kim, D. Han, H.S. Kim, K.Y. Chung, J. Mun, J. Kim, K.W. Nam, H. G. Jung, 2D Graphene-like carbon coated solid electrolyte for reducing inhomogeneous reactions of all-solid-State batteries, Adv. Energy Mater. 2403247 (2024) 1–13, https://doi.org/10.1002/aenm.202403247.
[18] Y. Kato, S. Hori, T. Saito, K. Suzuki, M. Hirayama, A. Mitsui, M. Yonemura, H. Iba, R. Kanno, High-power all-solid-state batteries using sulfide superionic conductors, Nat. Energy. 1 (2016) 16030, https://doi.org/10.1038/nenergy.2016.30.
[19] Y. Seino, T. Ota, K. Takada, A. Hayashi, M. Tatsumisago, A sulphide lithium super ion conductor is superior to liquid ion conductors for use in rechargeable batteries, Energy Environ. Sci. 7 (2014) 627–631, https://doi.org/10.1039/c3ee41655k.
[20] S. Yubuchi, M. Uematsu, M. Deguchi, A. Hayashi, M. Tatsumisago, Lithium-ion-conducting argyrodite-type Li6PS5X (X=Cl, Br, I) solid electrolytes prepared by a liquid-phase technique using ethanol as a solvent, ACS Appl. Energy Mater. 1 (2018) 3622–3629, https://doi.org/10.1021/acsaem.8b00280.
[21] N. Kamaya, K. Homma, Y. Yamakawa, M. Hirayama, R. Kanno, M. Yonemura, T. Kamiyama, Y. Kato, S. Hama, K. Kawamoto, A. Mitsui, A lithium superionic conductor, Nat. Mater. 10 (2011) 682–686, https://doi.org/10.1038/nmat3066.
[22] J. Kim, H. Lee, H. Cha, M. Yoon, M. Park, J. Cho, Prospect and reality of Ni-rich cathode for commercialization, Adv. Energy Mater. 8 (2018) 1–25, https://doi.org/10.1002/aenm.201702028.
[23] J. Wang, Z. Zhang, J. Han, X. Wang, L. Chen, H. Li, F. Wu, Interfacial and cycle stability of sulfide all-solid-state batteries with Ni-rich layered oxide cathodes, Nano Energy. 100 (2022) 107528, https://doi.org/10.1016/j.nanoen.2022.107528.
[24] S.H. Jung, U.H. Kim, J.H. Kim, S. Jun, C.S. Yoon, Y.S. Jung, Y.K. Sun, Ni-rich layered cathode materials with electrochemo-mechanically compliant microstructures for all-solid-State Li batteries, Adv. Energy Mater. 10 (2020) 1–12, https://doi.org/10.1002/aenm.201903360.

[25] R. Koerver, I. Aygün, T. Leichtweiß, C. Dietrich, W. Zhang, J.O. Binder, P. Hartmann, W.G. Zeier, J. Janek, Capacity fade in solid-State batteries: interphase formation and chemomechanical processes in nickel-rich layered oxide cathodes and lithium thiophosphate solid electrolytes, Chem. Mater. 29 (2017) 5574–5582, https://doi.org/10.1021/acs.chemmater.7b00931.

[26] S.K. Jung, H. Gwon, S.S. Lee, H. Kim, J.C. Lee, J.G. Chung, S.Y. Park, Y. Aihara, D. Im, Understanding the effects of chemical reactions at the cathode-electrolyte interface in sulfide based all-solid-state batteries, J. Mater. Chem. A. 7 (2019) 22967–22976, https://doi.org/10.1039/c9ta08517c.

[27] Y. Chen, L. Huang, D. Zhou, X. Gao, T. Hu, Z. Zhang, Z. Zhen, X. Chen, L. Cui, G. Wang, Elucidating and minimizing the space-charge layer effect between NCM cathode and Li6PS5Cl for sulfide-based solid-State lithium batteries, Adv. Energy Mater. 14 (2024) 1–14, https://doi.org/10.1002/aenm.202304443.

[28] L. Wang, R. Xie, B. Chen, X. Yu, J. Ma, C. Li, Z. Hu, X. Sun, C. Xu, S. Dong, T. S. Chan, J. Luo, G. Cui, L. Chen, In-situ visualization of the space-charge-layer effect on interfacial lithium-ion transport in all-solid-state batteries, Nat. Commun. 11 (2020) 1–9, https://doi.org/10.1038/s41467-020-19726-5.

[29] J. Haruyama, K. Sodeyama, L. Han, K. Takada, Y. Tateyama, Space-charge layer effect at interface between oxide cathode and sulfide electrolyte in all-solid-state lithium-ion battery, Chem. Mater. 26 (2014) 4248–4255, https://doi.org/10.1021/cm5016959.

[30] E. Hüger, L. Riedel, J. Zhu, J. Stahn, P. Heitjans, H. Schmidt, E. Hüger, L. Riedel, J. Zhu, J. Stahn, P. Heitjans, H. Schmidt, Lithium Niobate for fast cycling in Li-ion batteries: review and new experimental results, Batter 9 (2023) 244, https://doi.org/10.3390/BATTERIES9050244.

[31] A.Y. Kim, F. Strauss, T. Bartsch, J.H. Teo, J. Janek, T. Brezesinski, Effect of surface carbonates on the cyclability of LiNbO3-coated NCM622 in all-solid-state batteries with lithium thiophosphate electrolytes, Sci. Rep. 11 (2021) 1–9, https://doi.org/10.1038/S41598-021-84799-1;SUBJMETA=161,299,301,357,551,638,639,891,925;KWRD=BATTERIES,SYNTHESIS+AND+PROCESSING.

[32] X. Li, L. Jin, D. Song, H. Zhang, X. Shi, Z. Wang, L. Zhang, L. Zhu, LiNbO3-coated LiNi0.8Co0.1Mn0.1O2 cathode with high discharge capacity and rate performance for all-solid-state lithium battery, J. Energy Chem. 40 (2020) 39–45, https://doi.org/10.1016/j.jechem.2019.02.006.

[33] F. Walther, F. Strauss, X. Wu, B. Mogwitz, J. Hertle, J. Sann, M. Rohnke, T. Brezesinski, J. Janek, The working principle of a Li2CO3/LiNbO3Coating on NCM for thiophosphate-based all-solid-State batteries, Chem. Mater. 33 (2021) 2110–2125, https://doi.org/10.1021/acs.chemmater.0c04660.

[34] J.S. Lee, Y.J. Park, Comparison of LiTaO3and LiNbO3Surface layers prepared by post- and precursor-based coating methods for Ni-rich cathodes of all-solid-State batteries, ACS Appl. Mater. Interfaces 13 (2021), https://doi.org/10.1021/acsami.1c10294.

[35] N. Ohta, K. Takada, I. Sakaguchi, L. Zhang, R. Ma, K. Fukuda, M. Osada, T. Sasaki, LiNbO3-coated LiCoO2 as cathode material for all solid-state lithium secondary batteries, Electrochem. Commun. 9 (2007) 1486–1490, https://doi.org/10.1016/j.elecom.2007.02.008.

[36] W.S.K. Bong, A. Shiota, T. Miwa, Y. Morino, S. Kanada, K. Kawamoto, Effect of thickness and uniformity of LiNbO3-coated layer on LiNi0.5Co0.2Mn0.3O2 cathode material on enhancement of cycle performance of full-cell sulfide-based all-solid-state batteries, J. Power Sources. 577 (2023) 233259, https://doi.org/10.1016/J.JPOWSOUR.2023.233259.

[37] C. Wei, C. Yu, S. Chen, S. Chen, L. Peng, Y. Wu, S. Li, S. Cheng, J. Xie, Unraveling the LiNbO3 coating layer on battery performances of lithium argyrodite-based all-solid-state batteries under different cut-off voltages, Electrochim. Acta. 438 (2023) 141545, https://doi.org/10.1016/j.electacta.2022.141545.

[38] T. Shi, Y.Q. Zhang, Q. Tu, Y. Wang, M.C. Scott, G. Ceder, Characterization of mechanical degradation in an all-solid-state battery cathode, J. Mater. Chem. A. 8 (2020) 17399–17404, https://doi.org/10.1039/D0TA06985J.

[39] X. Liu, Y. Cheng, Y. Su, F. Ren, J. Zhao, Z. Liang, B. Zheng, J. Shi, K. Zhou, Y. Xiang, J. Zheng, M.S. Wang, J. Huang, M. Shao, Y. Yang, Revealing the surface-to-bulk degradation mechanism of nickel-rich cathode in sulfide all-solid-state batteries, Energy Storage Mater. 54 (2023) 713–723, https://doi.org/10.1016/j.ensm.2022.11.019.

[40] G.L. Gregory, H. Gao, B. Liu, X. Gao, G.J. Rees, M. Pasta, P.G. Bruce, C.K. Williams, Buffering volume change in solid-State battery composite cathodes with CO2-derived block polycarbonate ethers, J. Am. Chem. Soc. 144 (2022) 17477–17486, https://doi.org/10.1021/JACS.2C06138/ASSET/IMAGES/LARGE/JA2C06138_0006.JPEG.

[41] C. Liu, F. Roters, D. Raabe, Role of grain-level chemo-mechanics in composite cathode degradation of solid-state lithium batteries, Nat. Commun. 15 (2024) 1–18, https://doi.org/10.1038/s41467-024-52123-w.

[42] Y.J. Park, Y. Su, K. Yamamoto, T. Watanabe, N. Thakur, M. Kumar, T. Matsunaga, Y. Uchimoto, Unraveling the degradation mechanism of LiNbO3-coated NCM cathode at high potential in all-solid-State batteries using 10 K extended X-ray absorption fine structure analysis, Batter. Supercaps. 8 (2025) e202400697, https://doi.org/10.1002/BATT.202400697;REQUESTEDJOURNAL:JOURNAL:25666223;WGROUP:STRING:PUBLICATION.

[43] Y. Morino, S. Kanada, Degradation analysis by X-ray absorption spectroscopy for LiNbO3 coating of sulfide-based all-Solid-State battery cathode, ACS Appl. Mater. Interfaces. 15 (2023) 2979–2984, https://doi.org/10.1021/acsami.2c19414.

[44] L. Wang, A. Mukherjee, C.Y. Kuo, S. Chakrabarty, R. Yemini, A.A. Dameron, J. W. DuMont, S.H. Akella, A. Saha, S. Taragin, H. Aviv, D. Naveh, D. Sharon, T. S. Chan, H.J. Lin, J.F. Lee, C. Te Chen, B. Liu, X. Gao, S. Basu, Z. Hu, D. Aurbach, P. G. Bruce, M. Noked, High-energy all-solid-state lithium batteries enabled by Co-free LiNiO2 cathodes with robust outside-in structures, Nat. Nanotechnol. 19 (2024) 208–218, https://doi.org/10.1038/s41565-023-01519-8.

[45] F. Walther, R. Koerver, T. Fuchs, S. Ohno, J. Sann, M. Rohnke, W.G. Zeier, J. Janek, Visualization of the interfacial decomposition of composite cathodes in argyrodite-based all-solid-State batteries using time-of-flight secondary-ion mass spectrometry, Chem. Mater. 31 (2019) 3745–3755, https://doi.org/10.1021/acs.chemmater.9b00770.

[46] T.T. Zuo, F. Walther, J.H. Teo, R. Rueß, Y. Wang, M. Rohnke, D. Schröder, L. F. Nazar, J. Janek, Impact of the chlorination of lithium argyrodites on the electrolyte/cathode interface in solid-State batteries, Angew. Chemie - Int. Ed. 62 (2023), https://doi.org/10.1002/anie.202213228.

[47] G. Kresse, J. Furthmüller, Efficiency of ab-initio total energy calculations for metals and semiconductors using a plane-wave basis set, Comput. Mater. Sci. 6 (1996) 15–50, https://doi.org/10.1016/0927-0256(96)00008-0.

[48] P.E. Blöchl, Projector augmented-wave method, Phys. Rev. B. 50 (1994) 17953–17979, https://doi.org/10.1103/PhysRevB.50.17953.

[49] J.P. Perdew, K. Burke, M. Ernzerhof, Generalized gradient approximation made simple, Phys. Rev. Lett. 77 (1996) 3865, https://doi.org/10.1103/PhysRevLett.77.3865.

[50] A. Jain, G. Hautier, S.P. Ong, C.J. Moore, C.C. Fischer, K.A. Persson, G. Ceder, Formation enthalpies by mixing GGA and GGA + U calculations, Phys. Rev. B - Condens. Matter Mater. Phys. 84 (2011) 045115, https://doi.org/10.1103/PHYSREVB.84.045115/FIGURES/5/MEDIUM.

[51] G. Henkelman, B.P. Uberuaga, H. Jónsson, B.P. Uberuaga, H. Jó, A climbing image nudged elastic band method for finding saddle points and minimum energy paths, J. Chem. Phys. 113 (2000) 9901–9904, https://doi.org/10.1063/1.1329672.

[52] S.P. Ong, W.D. Richards, A. Jain, G. Hautier, M. Kocher, S. Cholia, D. Gunter, V. L. Chevrier, K.A. Persson, G. Ceder, Python Materials Genomics (pymatgen): a robust, open-source python library for materials analysis, Comput. Mater. Sci. 68 (2013) 314–319, https://doi.org/10.1016/J.COMMATSCI.2012.10.028.

[53] W.D. Richards, L.J. Miara, Y. Wang, J.C. Kim, G. Ceder, Interface stability in solid-State batteries, Chem. Mater. 28 (2016) 266–273, https://doi.org/10.1021/ACS.CHEMMATER.5B04082/ASSET/IMAGES/LARGE/CM-2015-04082X_0005.JPEG.

[54] T.Y. Pan, N.T.T. Tran, Y.C. Chang, W.D. Hsu, First-principles study on the initial reactions at LiNi1/3Co1/3Mn1/3O2 cathode/electrolyte interface in lithium-ion batteries, Appl. Surf. Sci. 507 (2020) 144842, https://doi.org/10.1016/J.APSUSC.2019.144842.

[55] C.Y. Son, D. Kim, S.Y. Jun, H. Park, W.H. Ryu, Asymmetrical functionalization of polarizable interface restructuring molecules for rapid and longer operative lithium metal batteries, Small 20 (2024) 2405143, https://doi.org/10.1002/SMLL.202405143.

[56] K. Momma, F. Izumi, VESTA3 for three-dimensional visualization of crystal, volumetric and morphology data, Urn:Issn:0021-8898. 44 (2011) 1272–1276. https://doi.org/10.1107/S0021889811038970.

[57] B. Wang, Y. Zhao, M.N. Banis, Q. Sun, K.R. Adair, R. Li, T.K. Sham, X. Sun, Atomic layer deposition of lithium niobium oxides as potential solid-State electrolytes for lithium-ion batteries, ACS Appl. Mater. Interfaces. 10 (2018) 1654–1661, https://doi.org/10.1021/acsami.7b13467.

[58] G. Lu, W. Peng, Y. Zhang, X. Wang, X. Shi, D. Song, H. Zhang, L. Zhang, Study on the formation, development and coating mechanism of new phases on interface in LiNbO3-coated LiCoO2, Electrochim. Acta. 368 (2021) 137639, https://doi.org/10.1016/J.ELECTACTA.2020.137639.

[59] X. Sun, S. Hori, Y. Li, Y. Yamada, K. Suzuki, M. Hirayama, R. Kanno, Annealing-induced evolution at the LiCoO2/LiNbO3 interface and its functions in all-solid-state batteries with a Li10GeP2S12 electrolyte, J. Mater. Chem. A. 9 (2021) 4117–4125, https://doi.org/10.1039/D0TA09313K.

[60] B. Wang, Y. Zhao, M.N. Banis, Q. Sun, K.R. Adair, R. Li, T.K. Sham, X. Sun, Atomic layer deposition of lithium niobium oxides as potential solid-State electrolytes for lithium-ion batteries, ACS Appl. Mater. Interfaces. 10 (2018) 1654–1661, https://doi.org/10.1021/ACSAMI.7B13467.

[61] P. Heitjans, M. Masoud, A. Feldhoff, M. Wilkening, NMR and impedance studies of nanocrystalline and amorphous ion conductors: lithium niobate as a model system, Faraday Disc. 134 (2006) 67–82, https://doi.org/10.1039/B602887J.

[62] K.B. Hatzell, X.C. Chen, C.L. Cobb, N.P. Dasgupta, M.B. Dixit, L.E. Marbella, M. T. McDowell, P.P. Mukherjee, A. Verma, V. Viswanathan, A.S. Westover, W. G. Zeier, Challenges in lithium metal anodes for solid-State batteries, ACS Energy Lett. 5 (2020) 922–934, https://doi.org/10.1021/ACSENERGYLETT.9B02668/ASSET/IMAGES/LARGE/NZ9B02668_0004.JPEG.

[63] P. He, Y. Tang, Z. Tan, C. Lei, Z. Qin, Y. Li, Y. Li, Y. Cheng, F. Wu, Z. He, J. Zhao, Solid-state batteries encounter challenges regarding the interface involving lithium metal, Nano Energy. 124 (2024) 109502, https://doi.org/10.1016/j.nanoen.2024.109502.

[64] H. Wang, C. Yu, S. Ganapathy, E.R.H. Van Eck, L. van Eijck, M. Wagemaker, A lithium argyrodite Li6PS5Cl0.5Br0.5 electrolyte with improved bulk and interfacial conductivity, J. Power Sourc. 412 (2019) 29–36, https://doi.org/10.1016/J.JPOWSOUR.2018.11.029.

[65] W. Weppner, R.A. Huggins, Determination of the kinetic parameters of mixed-conducting electrodes and application to the system Li3Sb, J. Electrochem. Soc. 124 (1977) 1569–1578, https://doi.org/10.1149/1.2133112/XML.

[66] A.P. Nowak, B. Wicikowska, K. Trzciński, A. Lisowska-Oleksiak, Determination of chemical diffusion coefficient of lithium ions in ceramics derived from pyrolysed poly(1,2-dimethylsilazane) and starch, Procedia Eng. 98 (2014) 8–13, https://doi.org/10.1016/j.proeng.2014.12.480.

[67] J. Lee, K. Nam, B. Ku, M. Choi, M.K. Cho, S.Y. Jung, J. Min, J. Ahn, Y. Lee, S.Y. Lee, D. Lee, Y.S. Cho, D.S. Kwon, J.K. Yoo, J. Kang, J. Kim, 2D Phosphorene-decorated Ni-rich layered cathodes for high-power and high-energy Li-ion batteries, Adv.

Funct. Mater. (2025) e11385, https://doi.org/10.1002/ADFM.202511385;REQUESTEDJOURNAL:JOURNAL:16163028;WGROUP:STRING:PUBLICATION.
[68] S. Payandeh, F. Strauss, A. Mazilkin, A. Kondrakov, T. Brezesinski, Tailoring the $LiNbO_3$ coating of Ni-rich cathode materials for stable and high-performance all-solid-state batteries, Nano Res. Energy. 1 (2022) 9120016, https://doi.org/10.26599/NRE.2022.9120016.
[69] F. Walther, F. Strauss, X. Wu, B. Mogwitz, J. Hertle, J. Sann, M. Rohnke, T. Brezesinski, J. Janek, The working principle of a Li2CO3/LiNbO3 coating on NCM for thiophosphate-based all-solid-State batteries, Chem. Mater. 33 (2021) 2110–2125, https://doi.org/10.1021/ACS.CHEMMATER.0C04660.
[70] X. Li, L. Jin, D. Song, H. Zhang, X. Shi, Z. Wang, L. Zhang, L. Zhu, LiNbO3-coated LiNi0.8Co0.1Mn0.1O2 cathode with high discharge capacity and rate performance for all-solid-state lithium battery, J. Energy Chem. 40 (2020) 39–45, https://doi.org/10.1016/J.JECHEM.2019.02.006.
[71] Y. Li, C. Kim, Y. Cho, A.L. Musgrove, G.D. Parker, Y.F. Su, R.L. Sacci, X.Y. Yu, T. Zawodzinski, J. Nanda, G. Yang, Promising performance of sulfide catholytes compared to halide alternatives in NMC811 cathodes for sheet-type sulfide solid-state batteries, Energy Storage Mater. 80 (2025) 104385, https://doi.org/10.1016/J.ENSM.2025.104385.
[72] M. Jiang, D.L. Danilov, R.A. Eichel, P.H.L. Notten, A review of degradation mechanisms and recent achievements for Ni-rich cathode-based Li-ion batteries, Adv. Energy Mater. 11 (2021) 2103005, https://doi.org/10.1002/AENM.202103005.
[73] Y.K. Ahn, Y.N. Jo, W. Cho, J.S. Yu, K.J. Kim, Mechanism of capacity fading in the LiNi0.8Co0.1Mn0.1O2 cathode material for lithium-ion batteries, Energies 12 (2019) 1638, https://doi.org/10.3390/EN12091638.
[74] S. Ardizzone, C.L. Bianchi, M. Fadoni, B. Vercelli, Magnesium salts and oxide: an XPS overview, Appl. Surf. Sci. 119 (1997) 253–259, https://doi.org/10.1016/S0169-4332(97)00180-3.
[75] V.V. Atuchin, I.E. Kalabin, V.G. Kesler, N.V. Pervukhina, Nb 3d and O 1s core levels and chemical bonding in niobates, J. Electron Spectros. Relat. Phenomena. 142 (2005) 129–134, https://doi.org/10.1016/J.ELSPEC.2004.10.003.